ADVANCING EARTH AND SPACE SCIENCE

Journal of Geophysical Research: Oceans

RESEARCH ARTICLE

10.1029/2018JC013794

Key Points:
- Observations show subduction of shelf water at the onshore edge of a warm-core ring that impinges on the Mid-Atlantic Bight shelf break
- The submesoscale frontal subduction of the shelf water at the shelf break results from the frontogenesis process on the ring edge
- The subducted shelf water is transported offshore underneath a surface layer of ring water by the strong ring-edge current

Correspondence to:
W. G. Zhang,
wzhang@whoi.edu

Citation:
Zhang, W. G., & Partida, J. (2018). Frontal subduction of the Mid-Atlantic Bight shelf water at the onshore edge of a warm-core ring. *Journal of Geophysical Research: Oceans*, *123*, 7795–7818. https://doi.org/10.1029/2018JC013794

Received 14 JAN 2018
Accepted 4 OCT 2018
Accepted article online 15 OCT 2018
Published online 5 NOV 2018

Frontal Subduction of the Mid-Atlantic Bight Shelf Water at the Onshore Edge of a Warm-Core Ring

Weifeng G. Zhang[1] and **Jacob Partida**[2]

[1]Applied Ocean Physics and Engineering Department, Woods Hole Oceanographic Institution, Woods Hole, MA, USA,
[2]Department of Oceanography and Department of Mathaematics, Humboldt State University, Arcata, CA, USA

Abstract This work studies the subduction of the shelf water along the onshore edge of a warm-core ring that impinges on the edge of the Mid-Atlantic Bight continental shelf. The dynamical analysis is based on observations by satellites and from the Ocean Observatories Initiative Pioneer Array observatory as well as idealized numerical model simulations. They together show that frontogenesis-induced submesoscale frontal subduction with order-one Rossby and Froude numbers occurs on the onshore edge of the ring. The subduction flow results from the onshore migration of the warm-core ring that intensifies the density front on the interface of the ring and shelf waters. The subduction is a part of the cross-front secondary circulation trying to relax the intensifying density front. The dramatically different physical and biogeochemical properties of the ring and shelf waters provide a great opportunity to visualize the subduction phenomenon. Entrained by the ring-edge current, the subducted shelf water is subsequently transported offshore below a surface layer of ring water and alongside of the surface-visible shelf-water streamer. It explains the historical observations of isolated subsurface packets of shelf water along the ring periphery in the slope sea. Model-based estimate suggests that this type of subduction-associated subsurface cross-shelfbreak transport of the shelf water could be substantial relative to other major forms of shelfbreak water exchange. This study also proposes that outward spreading of the ring-edge front by the frontal subduction may facilitate entrainment of the shelf water by the ring-edge current and enhances the shelf-water streamer transport at the shelf edge.

Plain Language Summary This study is based on measurements from satellites and the Ocean Observatories Initiative Pioneer Array observatory at the edge of the Mid-Atlantic Bight continental shelf. It shows an unusual form of downward flow (subduction) of the shelf water on the edge of a Gulf Stream warm-core ring that migrates toward the shallow continental shelf. Computer simulations reproduce the observed phenomenon and reveal the underlying mechanism: the onshore migration of the warm-core ring sharpens the interface of the ring and shelf waters; the subduction flow is a part of the cross-sectional circulation trying to relax the sharpening interface. The dramatically different physical and chemical properties of the ring and shelf waters help visualize the phenomenon. The subducted shelf water is then carried into the deep sea underneath a surface layer of warm-core ring water by the strong ring current. This offshore flow of the shelf water represents a type of water exchange process at the shelf edge that can potentially be significant but has not been well studied. It does not have a surface signature and cannot be seen by satellites. The subsurface measurements from the Pioneer Array observatory provide a great opportunity for this study.

1. Introduction

1.1. Mid-Atlantic Bight Shelfbreak Circulation

The Mid-Atlantic Bight (MAB) shelf break off the U.S. northeast coast sits between the relatively cold, fresh shelf water and the warm, saline offshore waters (e.g., Chapman & Beardsley, 1989; Houghton et al., 2009; Linder & Gawarkiewicz, 1998). A prominent *retrograde* shelfbreak density front (isopycnals shoaling toward offshore) marks the boundary between the shelf and slope waters, with clear temperature and salinity signatures (e.g., Houghton et al., 1988; Zhang et al., 2011). The shelf water is generally less dense than the slope water, as the shelfbreak salinity difference often dominates the density variation. However, the cross-shelfbreak density gradient can be reversed, especially at times of Gulf Stream warm-core rings (WCRs) impinging on the shelf edge (e.g., Zhang & Gawarkiewicz, 2015a) forming a *prograde* density front (isopycnals shoaling toward inshore). The dramatic temperature difference between the shelf and ring waters can outweigh the salinity effect and make the shelf water denser than the adjacent ring water.

In this study, the waters in the shelfbreak region are divided into three general categories: (i) shelf water, defined as *potential* temperature <14°C and *absolute* salinity <34.7 g/kg, corresponding to the water onshore of the MAB shelfbreak front in springtime (Linder & Gawarkiewicz, 1998; Zhang et al., 2011); (ii) ring water with near-surface *potential* temperature >19°C and *absolute* salinity >36 g/kg; and (iii) slope water with properties between. Note that salinity presented here is absolute salinity (McDougall et al., 2012).

Despite the topographic constraint and the shelfbreak front, there is onshore and offshore transport of waters across the shelf edge, representing the exchange of the shelf and offshore waters that is important for the heat and salt balances on the continental shelf (Lentz, 2008). There are different types of shelfbreak exchange, including surface Ekman transport (Gawarkiewicz et al., 1996), pycnocline onshore intrusion of the slope water (Lentz, 2003), frontal eddy transport (Gawarkiewicz et al., 2004), Pinochio's Nose onshore intrusion (PNI) of the WCR water (Zhang & Gawarkiewicz, 2015a), and shelf-water offshore streamer transport (e.g., Garfield & Evans, 1987; Joyce, 1991).

Both the PNI and streamers have distinct surface signatures that are visible to satellites. The former is an elongated feature of WCR water extending equatorward along the shelf break, and the latter is a cold filament of shelf water wrapping around the WCR in the slope sea. They both can transport a substantial amount of water across the shelf break. The onshore transport of ring water in a 2014 PNI event was ~0.22 Sv (Zhang & Gawarkiewicz, 2015a); the cross-shelfbreak offshore transport of the shelf water in a 2006 streamer was ~0.28 Sv (Chen et al., 2014). Studies argued that the shelf-water streamer results from entrainment by the WCR (e.g., Joyce et al., 1992; Schlitz, 2003). Using a model with no shelfbreak front and no distinction between the shelf and slope waters, Cherian and Brink (2016, 2018) showed that the entrainment of the water on the shelf by the WCR is a barotropic process driven by onshore motion of the ring water. When applied to the northern MAB (Figure 1), the barotropic process would create a northeastward sea level setdown in the ring-shelf contact region. The associated barotropic pressure gradient force to the north of the WCR would drive an eastward jet of several tens of kilometer (~40 km for MAB) wide through the geostrophic balance and move shelf water toward the streamer; the eastward barotropic pressure gradient force at the eastern end of the ring-shelf contact region would drive an offshore flow of the shelf water and form the streamer. But how the strong baroclinicity at the MAB shelf break, particularly, the presence of the shelfbreak front, affects this shelf-water entrainment process remains unclear.

The WCR-induced cross-shelfbreak offshore transport of the shelf water can also occur below the sea surface. Observations have shown subsurface fluxes of shelf water on the ring periphery alongside of surface-visible shelf-water streamers (e.g., Churchill et al., 1986; Kupferman & Garfield, 1977; Tang et al., 1985). The model of Cherian and Brink (2016) produces a type of subsurface offshore flux of the shelf-slope water, and they attribute it to the along-isopycnal sinking of the shelf-slope water. But no mechanism is provided to explain the along-isopycnal sinking, and the dynamics of the WCR-induced subsurface shelf-water offshore transport remains unclear. This study focuses on the subsurface cross-shelfbreak offshore transport of the shelf water that starts with frontogenesis-induced shelf water subduction at the *prograde* density front along the northern edge of an onshore-impinging WCR. Note that the ring edge here refers to the temperature and salinity boundary of the ring where the velocity starts to increase.

1.2. Frontal Subduction and Filament

The dynamics of frontal subduction has been investigated in the atmosphere and open ocean as an ageostrophic, submesoscale phenomenon associated with frontogenesis (e.g., Hoskins, 1982; Levy et al., 2001; Mahadevan & Tandon, 2006; Spall, 1995). An ocean submesoscale phenomenon is characterized by Rossby number,

$$Ro = \frac{U}{fL_c}, \tag{1}$$

and Froude number

$$Fr = \frac{U}{NH}, \tag{2}$$

both being $O(1)$ (McWilliams, 2016). Here U is the frontal velocity scale, f is the Coriolis parameter, N is the buoyancy frequency, and L_c and H are the cross-frontal and vertical length scales of the submesoscale

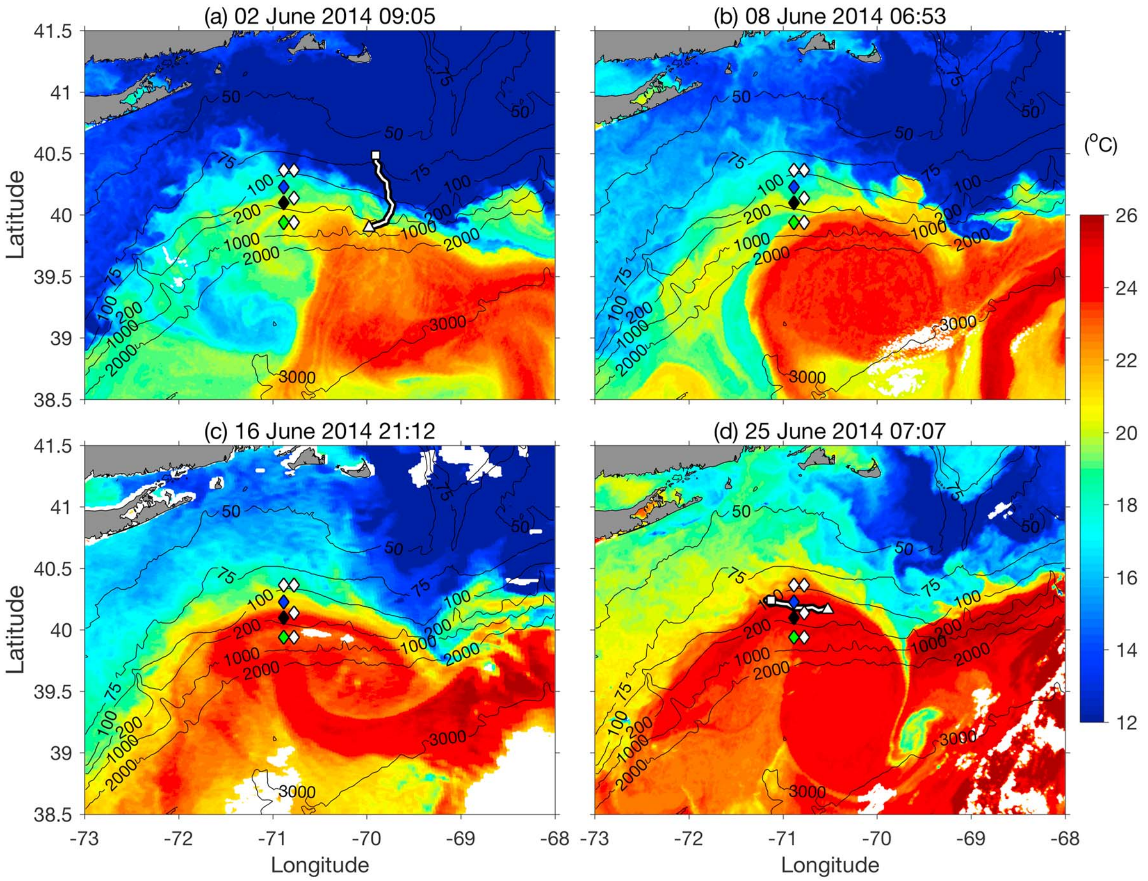

Figure 1. (a–d) Satellite-measured sea surface temperature in the northern Mid-Atlantic Bight region at four different times in June 2016. The white areas represent cloud cover. The thin black lines are isobath contours. The diamonds indicate locations of the Ocean Observatories Initiative Pioneer Array moorings with the green, black, and blue filled ones representing the Offshore, Central Offshore and Central Inshore moorings, respectively; the thick white line in (a) is the track of the EB glider transect shown in Figure 4; the thick white line in (d) is the track of the FZ glider transect shown in Figure 7 right column. The triangles and squares represent the beginning and end of the transects, respectively.

frontal subduction, respectively. Furthermore, L_c is generally smaller than the first baroclinic Rossby radius of deformation

$$L_R = \frac{NH_r}{f}, \tag{3}$$

where H_r is the vertical length scale of the mesoscale process (e.g., WCRs). H_r is generally greater than the vertical length scale of submesoscale processes, that is, $H_r > H$.

The vertical flow associated with ageostrophic frontal subduction can transport surface tracers downward creating slanted three-dimensional (3-D) *along-isopycnal* tracer filaments with strong horizontal gradients (Omand et al., 2015). A related but different process is the horizontal stirring of a geostrophic shear flow that, even with no vertical velocity, can strain the tracer field, intensify existing along-isopycnal tracer gradients (e.g., spiciness) at depth, and result in subsurface, slanted, *cross-isopycnal*-appearing tracer filament (Smith & Ferrari, 2009). The increase of the tracer horizontal gradient by this geostrophic shear stirring can be described as

$$\frac{D(\nabla, C)}{Dt} = -\boldsymbol{\sigma}\nabla C, \tag{4}$$

where C is the tracer concentration, $\sigma_{ij} \equiv \partial u_i/\partial x_j$ is the horizontal strain tensor, and $\nabla = (\partial x, \partial y, \partial z)$. Presumably, geostrophic shear stirring and frontal subduction could occur simultaneously in a frontal region and form subsurface slanted 3-D tracer layers.

At the MAB shelf break, bathymetry exerts strong influence on circulation (e.g., Cherian & Brink, 2016; Zhang & Gawarkiewicz, 2015b). Whether the bathymetry can affect the frontal subduction and modify the influence of geostrophic shear stirring is unclear. This study shows that the frontal behaviors at the shelf break are similar to those in the open ocean and that shelf water is subducted at the intensifying density front at the onshore edge of the WCR and then transported offshore. The shelf-water subduction and cross-shelfbreak offshore transport occur beneath a surface layer of ring water and thus cannot be detected by satellites. Subsurface measurements of the Ocean Observatories Initiative (OOI) Pioneer Array observatory at the northern MAB shelf break (Smith et al, 2018) provide a great opportunity for studies of the frontal subduction process.

2. Methods

2.1. Observations

This study uses data from satellites and the OOI Pioneer Array. Sea surface temperature (SST) from single-pass snapshots taken by different satellites with a horizontal resolution of 1 km is used here to provide the regional context. The different surface temperature of the ring, slope, and shelf waters during the study period of June 2014 make SST an effective tool for distinguishing the water masses.

In situ measurements in June 2014 from the Pioneer Array, including temperature, salinity, dissolved oxygen (DO), and colored dissolved organic matter (CDOM), and velocity data from McLane moored profilers at the Central Inshore (CI), Central Offshore (CO), and Offshore (OS) moorings and from the Eastern Boundary (EB) and Frontal Zone (FZ) gliders, are downloaded from the NSF OOI data portal (http://ooinet.oceanobservatories.org) and presented here. The CI, CO, and OS moorings are located on the western mooring line of 70.883°W at respective water depths of 127, 147, and 450 m (Figure 1). The McLane profilers on them take a vertical profile every 1.5, 1.5, and 3 hr, respectively, and the downloaded data have a vertical resolution of 1.5 m. The cross-shelf EB glider line is located 80 km to the east of the moorings (Figure 1b); the FZ glider line is oriented in the along-shelf direction (Figure 1d). The gliders sample the water column with the horizontal interval of 200–2,000 m, depending on the local water depth, and report data in the vertical resolution of 0.3 m.

The ADCP horizontal velocity data from the CO mooring are presented here to show the ring-edge flow. The ADCP has the vertical bin size of 4 m and the time-average window of 15 min. A low-pass filter with a 5-day Lanczos window (with half-power point at ±1.5 days) is applied to the ADCP data at each depth to remove the strong internal wave signals that are ubiquitous in the Pioneer Array velocity data and hinder the data interpretation. This filter not only removes the internal wave signals but also smooths the signals associated with the fast-moving ring edge. However, because the ring signal lasts for at least several days, the lower frequency signature of the WCR remains visible (see below). We here present both raw and filtered horizontal velocity data with u and v representing eastward and northward components of the velocity, respectively.

2.2. Modeling

The Regional Ocean Modeling System (Shchepetkin & McWilliams, 2008) with an idealized configuration is used in this study. The model solves nonlinear Boussinesq hydrostatic momentum equations and a single density equation. The model configuration is similar to that in Zhang and Gawarkiewicz (2015a, 2015b). It has an idealized rectangular domain with the area of 2,010.5 km (in x and along-shelf) × 479 km (in y and cross-shelf). The origin of the coordinate is at the center point of the northern coastal boundary. The model horizontal resolution is 500 m in both x and y directions in the central study region of 500 km × 350 km and decreases to 2 km on the outer boundaries. There are 60 terrain-following vertical layers with thinner layers toward the surface and bottom. The model bathymetry is uniform in the along-shelf (x) direction. Its cross-shelf variation in y direction is an idealized MAB shelfbreak bathymetry (Figure 2b):

$$h = \max\left(0, h_f \frac{y_p + l_f - y}{y_p + l_f}\right) + h_{p1} \tanh \frac{y - y_p}{l_p} - h_{p2}. \tag{5}$$

Here the shelf width scale $l_f = 41$ km, y coordinate of the center of the slope $y_p = -170.5$ km, the cross-shelf length scale of the slope $l_p = 16.5$ km, the shelf depth scale $h_f = 65$ m, and the slope vertical scales $h_{p1} = 465$ m

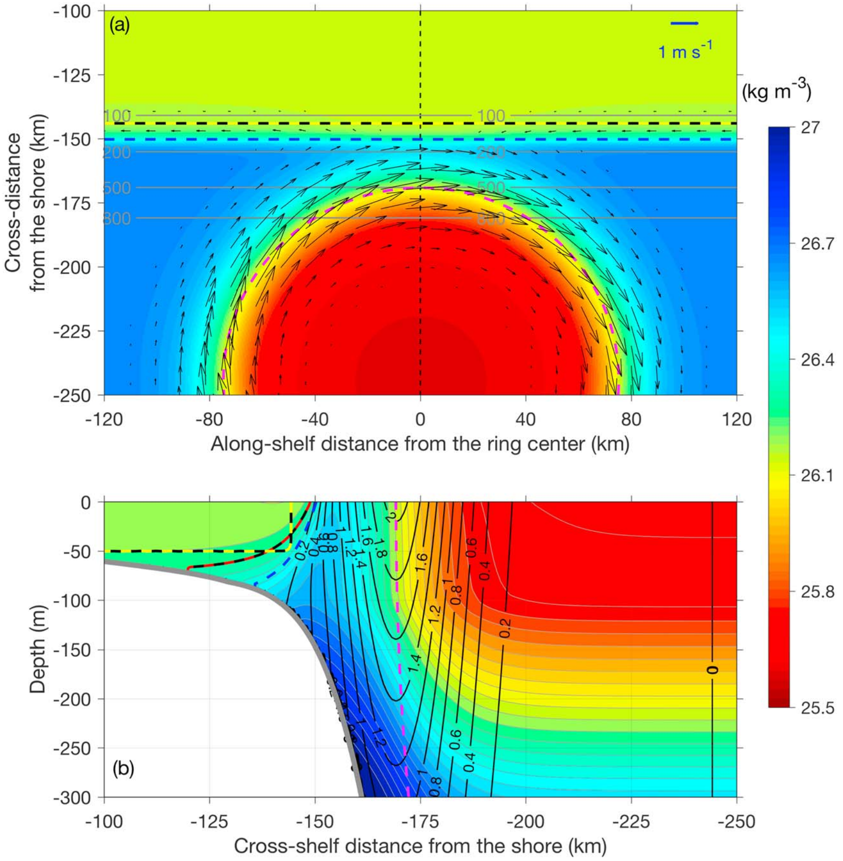

Figure 2. Model initial density (color) and velocity (vectors in (a) and black contours in (b)) fields on the (a) surface and (b) the cross-shelf section going through the center of the warm-core ring (the dashed black line in (a)). The velocity scale is provided at the top-right corner of (a). The dashed blue, black-yellow, and magenta lines are the edges of the shelf (C_s), surface-shelf (C_{s2}), and warm-core ring (C_r) waters, respectively. The dashed black-red line in (b) highlights the isopycnal of 26.3 kg/m^3 on the shelf, which intercepts the boundary of C_{s2} (the dashed black-yellow line). The grey lines in (a) are isobath contours. Note that the thermal-wind-balanced, westward, initial shelfbreak front jet exists throughout the along-shelf extent of the model domain. It does not show up on the velocity contour in (b) because it is weakened in the central region of the domain ($x \in (-40, 40$ km)) by the subsurface prograde isopycnal tilt associated with the ring.

and $h_{p2} = 540$ m. The bathymetry starts from 10-m deep on the northern coast, deepens southward with a slope of $\alpha \approx 0.5 \times 10^{-3}$ to the 100-m isobath at $y \approx -140$ km, and then transitions to a hyperbolic-tangent-shaped continental slope with a maximum depth of 1,005 m.

Along-shelf periodic boundary conditions are applied in all simulations. Horizontal explicit viscosity and diffusivity are 0 in the 500 km × 350 km study area and increase outward reaching 100 m^2/s on the western, southern, and eastern boundaries. A general length scale vertical turbulence closure *k-kl* scheme (Warner et al., 2005) and quadratic bottom drag with coefficient of 0.003 are used. There is no surface forcing.

The model initial density consists of an idealized retrograde shelfbreak front separating the shelf and slope waters and an idealized circular WCR residing in the slope water (Figure 2). The density of the slope water is horizontally uniform and varies vertically. Its vertical profile is based on an observed profile in the MAB slope sea with surface density of $\rho_{sl} = 1{,}026.7$ kg/m^3. The shelf water with surface density of ρ_{sh} is characterized by negative, along-shelf uniform density anomaly relative to the slope water. The cross-shelf density gradient forms a shelfbreak front with isopycnals rising from the ocean floor toward offshore (Zhang & Gawarkiewicz, 2015b).

The WCR has a density anomaly relative to the slope water (Figure 2) specified by

Table 1
Model Sensitivity Parameters

Symbol	Sensitivity parameter	Unit	Values[a]
$\Delta\rho_0$	Surface density anomaly of the ring water	kg/m^3	-0.5; -0.75; $-$**1**; -1.25
y_0	Cross-shelf location of the ring center	km	-240; $-$**245**; -250; -255
β	Northward gradient of Coriolis Parameter ($\partial f/\partial y$)	10^{-11} (m s)$^{-1}$	-1.76; **0**; 1.76

[a] The control values of the parameters are highlighted in bold.

$$\Delta\rho_r(x,y,z)=\frac{1}{2}\left[1-\tanh\left(\frac{r-r_c}{r_b}\right)\right]e^{-\frac{z^2}{H_r^2}}\Delta\rho_0. \tag{6}$$

Here $\Delta\rho_0$ is the surface density anomaly at the ring center, (x_0, y_0); $r = [(x\text{-}x_0)^2 + (y\text{-}y_0)^2]^{1/2}$; r_c is the ring radius to the maximum velocity; r_b is the horizontal length scale of the ring-edge transition region; H_r is the ring vertical scale.

In the control simulation $f = f_0 = 9.37 \times 10^{-5}$ s^{-1} (40°N; f-plane); $\rho_{sh} = 1{,}026.2$ kg/m^3; $x_0 = 0$ km and $y_0 = -245$ km; $r_c = 75$ km, $r_b = 15$ km; $H_r = 500$ m; $\Delta\rho_0 = -1$ kg/m^3, resembling the observed density difference between the ring and slope waters. These parameters together give a Burger number of the ring, $NH_r/(fr_c)$, of about 0.7. Here $N \approx 0.01$ s^{-1}. The surface density of the ring water $\rho_r = \rho_{sl} + \Delta\rho_0 = 1{,}025.7$ kg/m^3. On the sea surface $\rho_r < \rho_{sh} < \rho_{sl}$, consistent with the observed density contrasts among the ring, shelf, and slope waters (Zhang & Gawarkiewicz, 2015a). The density distribution across the shelfbreak front resembles a typical MAB shelfbreak frontal structure in winter and spring (e.g., Fratantoni et al., 2001; Gawarkiewicz et al., 2001).

Thermal-wind balanced horizontal velocity (assuming zero bottom velocity) and geostrophically balanced sea level tilt are added to the model initial conditions. The ring initially sits on the slope and is not completely balanced, as the thermal-wind assumption neglects the centrifugal force and the zero-velocity assumption on the sloping bottom induces cross-shelf flow asymmetry. However, the ring adjusts itself dynamically in the first several days before the frontal subduction occurs (see below), and the details of the initial ring flow condition is not expected to alter the result here. To facilitate the perturbation growth, Gaussian random velocity perturbation with zero mean and standard deviation of 0.02 m/s is added to the ring current. Because this study focuses on the development of the ring-edge frontal subduction, all simulations are run for only 20 days (25 inertial periods), long enough to capture the shelf-water subduction phenomenon and the initial cross-shelfbreak offshore transport.

Three passive tracers, representing ring, shelf, and surface shelf waters with concentration C_r, C_s, and C_{s2}, respectively, are included in the model. The passive tracer equation is the same as the density equation except with no feedback to the circulation. The initial value of C_r is 1 in the WCR and 0 elsewhere (the dashed magenta line in Figure 2 represents the boundary). The initial value of C_s is 1 in the shelf water and 0 elsewhere with the boundary (dashed blue line in Figure 2) aligning with a shelf water isopycnal. The initial concentration of C_{s2} is 1 in the top 50 m of the shelf onshore of $y = -144$ km and 0 elsewhere, and its boundary (dashed black-yellow line in Figure 2) intercepts the isopycnal $\sigma_\theta = 26.3$ kg/m^3 (dashed black-red line in Figure 2b). Note that C_s has no initial along-isopycnal variation and C_{s2} does. This difference has important dynamical consequence and helps explain the cross-isopycnal characteristics of the subduction signal (section 4). Sensitivity simulations (Table 1) with varying ring-water density ($\Delta\rho_0$), cross-shelf position of the ring (y_0), and spatially varying f ($f = f_0 + \beta y$) are also conducted.

3. Observational Analysis

3.1. General Pattern

SST in June 2014 shows the impingement of a WCR on the shelf edge (Figure 1). On 2 June, the WCR is located to the southeast of the Pioneer Array moorings. It then migrates westward with its northwestern edge reaching the OS mooring on 8 June. In the next 8 days, the northern edge of the ring migrates northward and

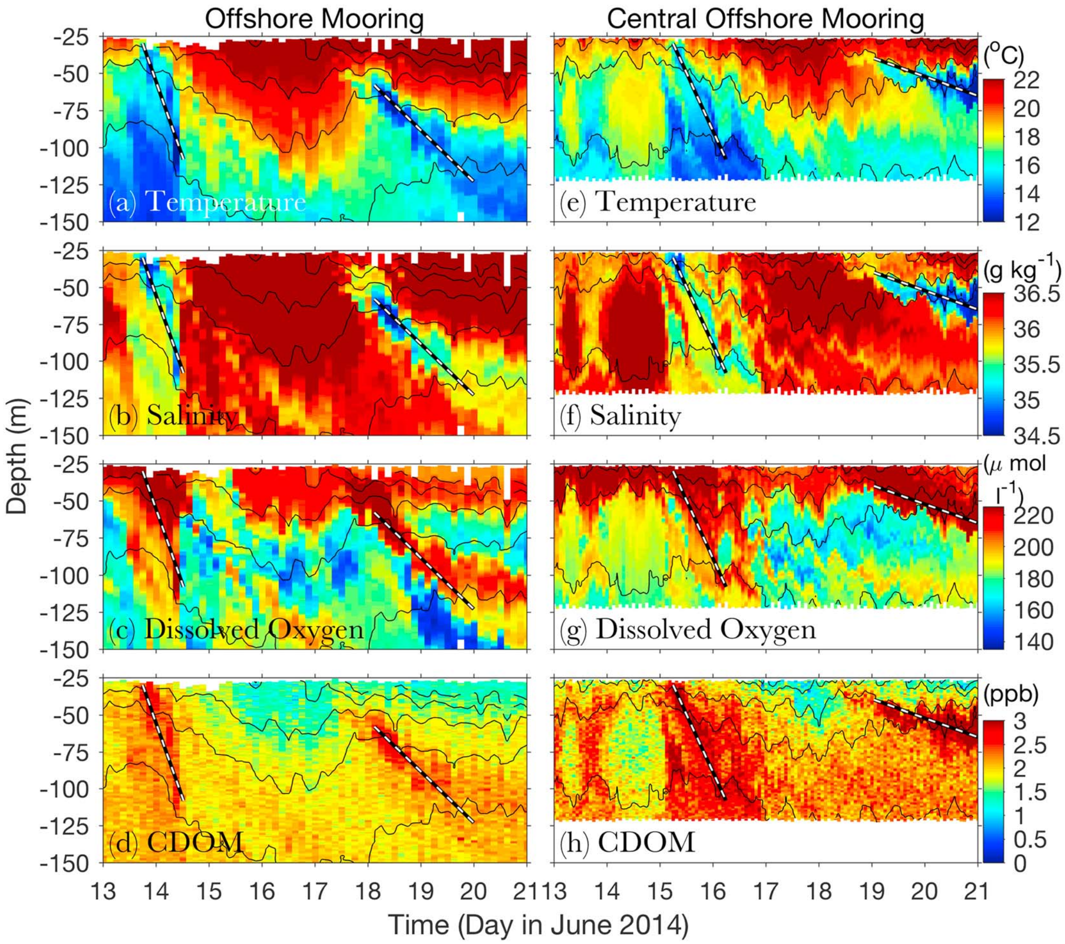

Figure 3. Temporal evolution of potential temperature, absolute salinity, dissolved oxygen, and colored dissolved organic matter concentration vertical profile measured at the (left) Offshore and (right) Central Offshore moorings on 13–21 June 2014. The solid lines in each panel are isopycnals with the contour interval of 0.5 kg/m^3. The dashed lines highlight the descending signals described in the text.

reaches the OS mooring on 16 June. Meanwhile, a shelf-water streamer developed to the east of the ring with a cold (~18 °C) patch transported offshore reaching 39.2°N on 25 June (Figure 1d).

Time series data at both CO and OS moorings during the period of the ring impingement show episodic filaments with apparent downward signal propagation on the period of 1–2 days, as highlighted in Figure 3. In particular, relatively cold (12–14 °C), fresh (34–35.7 g/kg), high oxygen (>210 μmol/kg), and high CDOM signals descends underneath the relatively warm, saline, low oxygen, and low CDOM ring water. Note that the apparent downward signal propagation does not necessarily represent downward water motion (see below). Also note that the high-frequency oscillations signals superposed on the descending signals mostly represent internal waves. The descending filaments appear on 13–14 and 18–19 June at the OS mooring (Figure 3, left) and on 15–16 and 19–20 June at the CO mooring (Figure 3, right). The filaments are ~20 m thick. During 13–14 June at the OS mooring and 15–16 June at the CO mooring, the filament signal propagates from $z = -30$ m to -110 m within a day. The corresponding vertical signal descending speed $|w_0| \approx 80$ m/day or 0.9 mm/s. The filament signal on 18–19 June at the OS mooring descends from $z = -60$ m to -120 m in 2 days with $|w_0| \approx 0.3$ mm/s. The signal on 19–20 June at the CO mooring descends from $z = -40$ to -70 m in 2 days with $|w_0| \approx 0.2$ mm/s.

Physical and biogeochemical signatures of the filaments indicate that they represent diluted near-surface shelf water. The relatively low temperature and salinity of the water suggest that it originates from the outer shelf. In particular, the initial salinity of descending signal is <34.7 (Figures 3b and 3g), so that at least part of

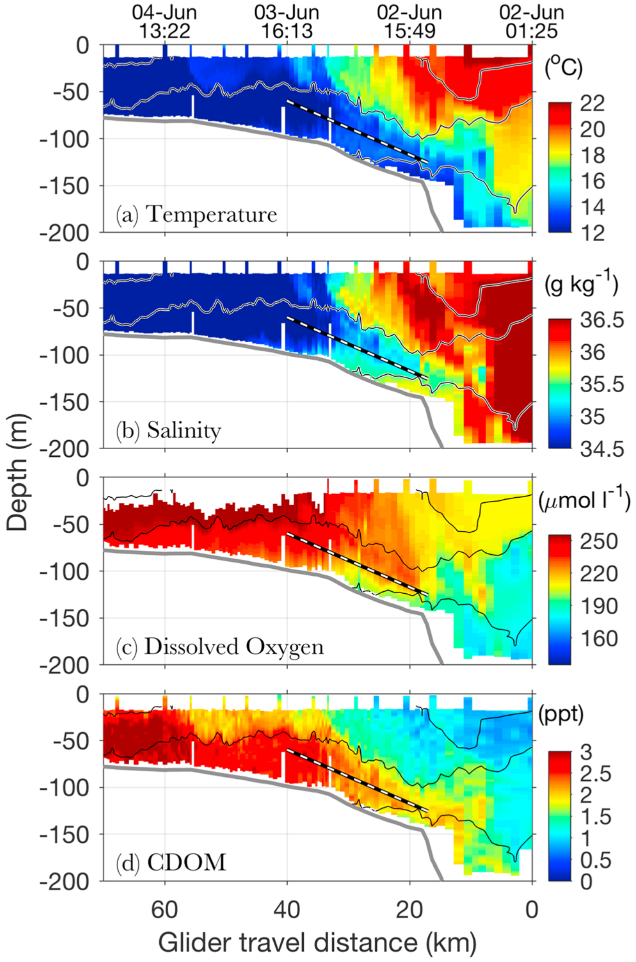

Figure 4. Cross-shelf sections of potential temperature, absolute salinity, dissolved oxygen, and colored dissolved organic matter measured by a Pioneer Array EB glider over 2–4 June 2014. The thin lines in each panel are isopycnals with the contour interval of 0.5 kg/m^3. The thick grey lines are the bottom. The tracks of the glider missions are shown in Figure 1a. The dashed lines highlight the subsurface layer of shelf water described in the text.

the water in the filaments is from the onshore side of the shelfbreak front. The relatively high concentration of DO indicates that the filament shelf water has recently been exposed to the surface. The relatively high concentration of CDOM is consistent with the shelf origin of the filament water. Because of relatively high biological productivity, the MAB shelf water generally has higher concentration of DO and CDOM than the offshore waters (Vaillancourt et al., 2005). Consistently, the EB glider cross-shelf section shows a general trend of decreasing concentration of DO and CDOM toward offshore (Figures 4c and 4d). Note that the CDOM concentration on the shelf also decreases slightly toward the surface, which is likely caused by photodegradation (Figure 4d).

Temperature-salinity (T-S) and oxygen-salinity (O-S) properties of the filament water suggest that the descending signals result from some type of downwelling flow. Because the filament water at the CO and OS moorings originates from the shelf side, it likely has passed through the CI mooring some time prior to reaching CO and OS moorings. Consistently, on the T-S and O-S diagrams, the deep filament waters at the CO and OS moorings overlap with the water at the CI mooring in May–June 2014 (Figure 5). But the filament waters at the CO and OS moorings are located at greater depths than the water at the CI mooring of the same T-S and O-S properties. The depth differences suggest that the deep filament water at the CO and OS moorings has been transported downward after passing through the CI mooring.

Velocity data at the CO mooring (Figure 6) indicate that the descending filaments appear at the same time as the arrivals of the onshore edge of the WCR where the frontal velocity starts to increase. Thus, the filaments likely represent a frontal process. A barotropic northward onshore flow and a surface-intensified eastward along-shelf flow appear on 15 June, approximately the same time as the first filament at the CO mooring (cf. Figure 3 right). As the ring edge near the moorings on 15–16 June is east-west oriented (cf. Figure 1c), the northward and the eastward flow represent a cross- and an along-front current, respectively. The onshore flow lasts for a day with the maximum speed (after the low-pass filter) of ~0.12 m/s. This onshore flow is presumably caused by the onshore migration of the ring edge pushing the entire water column shoreward. The eastward flow at the CO mooring persists for $>$6 days. During 16–17 June, the eastward (along-front) flow occupies the entire water column. The maximum eastward speed in the raw and low-pass filtered data is 1.22 and 0.48 m/s, respectively. This strong eastward flow means that the shelfbreak flow is not two-dimensional (cross-shelf and vertical) and that the observed filaments represent 3-D slanted sheets of cold and fresh water being advected eastward passing through the moorings by the ring-edge current. The measured cross-shelf velocity at the mid-depth changes its direction to offshore on 16 June and remains offshore for ~2 days. The filtered maximum offshore velocity of ~0.07 m/s occurs at $z = -50$ m. This subsurface-intensified offshore velocity may represent a secondary flow on the vertical section across the ring-edge front. However, no clear subsurface offshore flow appears in the raw data. A similar but weaker pattern of cross-shelf velocity variation exists on 18–20 June, coincident with the second filament at the CO mooring.

The EB glider cross-shelf transect on 2–4 June give a nonsynoptic cross-sectional view of the frontal feature (Figure 4). It depicts the cross-shelf transition from the ring water offshore to the shelf water onshore. The ring-edge isopycnals form a prograde front at the shelf break. It shows an intermediate layer of low temperature, low salinity, high DO, and high CDOM shelf water extending offshore and downward underneath the ring water, reaching $z = -120$ m, beyond the normal depth range of the shelf water. The cross-shelf length scale of the intermediate shelf-water layer is ~10 km. This intermediate layer is separated from the bottom by

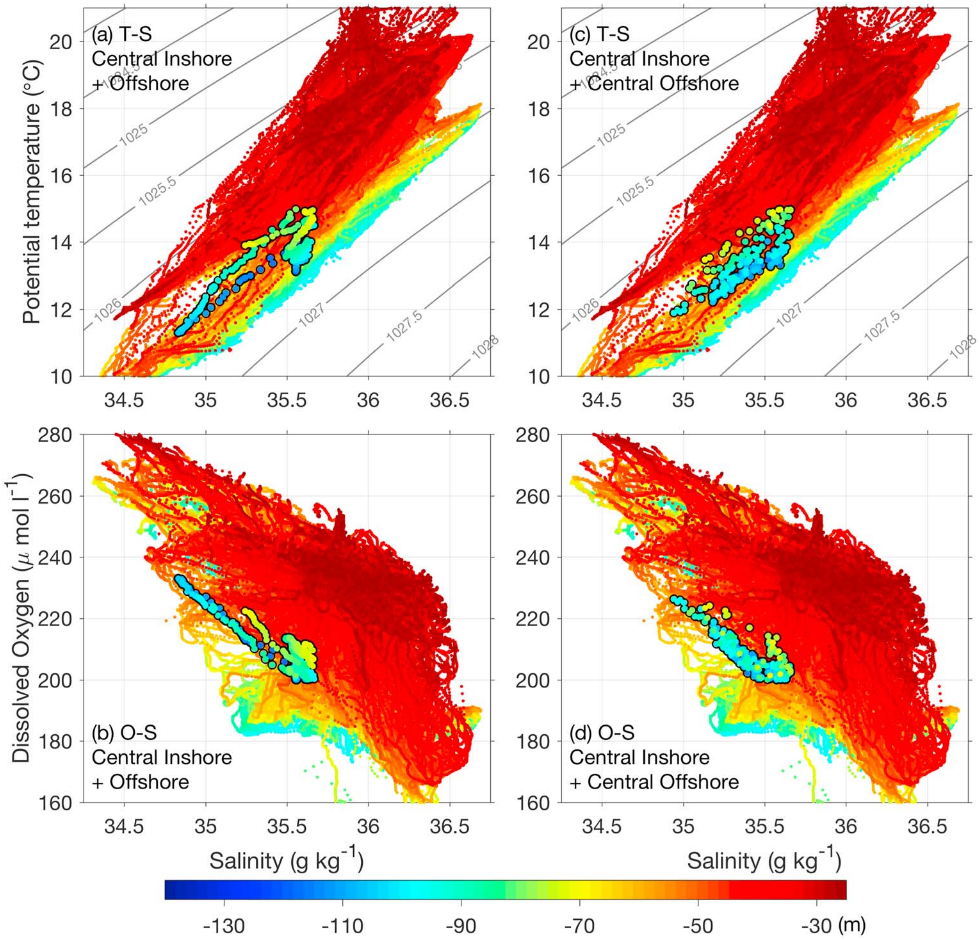

Figure 5. (top) Temperature-salinity and (bottom) Oxygen-salinity diagrams of the data measured by the Offshore (black-circled dots in the left column), Central Offshore (black-circled dots in the right column), and Central Inshore (small colored dots with no circles in both columns) mooring profilers. The color of the dots represents the depth of the measurements. For the Offshore mooring, only the data in the descending filaments on 13–14 June 2014 below $z = -70$ m (Figure 3 left) are shown; for the Central Offshore mooring, only the data in the descending filament on 15–17 June 2014 below $z = -70$ m (Figure 3 right) are shown; for the Central Inshore mooring, data at all depth within the period of 1 May to 21 June 2014 are shown.

a 10- to 20-m-thick bottom layer of low temperature, intermediate salinity, low DO, and low CDOM water. Consistent with the mooring data, the temperature and salinity at the shelf end of the intermediate layer (at the 100-m isobath) is ~12 °C and $<$34.7 g/kg, respectively; salinity in the intermediate layer increases gradually toward offshore. Other EB glider cross-shelf transects in the same region at different times in June 2014 show qualitatively similar layering pattern (not shown).

Data from the FZ glider along-shelf transect indicate that the frontal filament feature likely occurs over an extended along-shelf distance on the onshore ring edge. The CO mooring data show another descending filament on 23–25 June (Figure 7, left). The cold, fresh, and high DO filament layer later rests at the depth of $z = -80$ m after 25 June with much warmer and saltier water sitting above and slightly warmer and saltier water sitting below. Meanwhile, the FZ glider along-shelf transect near the CO mooring on 25–28 June show an ~20-m-thick subsurface layer of relatively fresh (34–35.7 g/kg), cold (11–15 °C), and high CDOM shelf water spanning over the along-shelf distance of ~60 km (Figure 7, right). This subsurface layer sits at the depth range of $z = -60$ to -80 m, below a surface layer of ring water of high temperature ($>$22 °C) and salinity ($>$36 g/kg) and above a bottom layer of slope water of intermediate temperature (~16 °C) and salinity ($>$35.7 and $<$36 g/kg). The middle layer presumably represents the filament water of diluted shelf source captured by the CO mooring. Its along-shelf span suggests that the filament likely extend in the along-shelf direction over a distance of $>$60 km, thus forming a 3-D sheet.

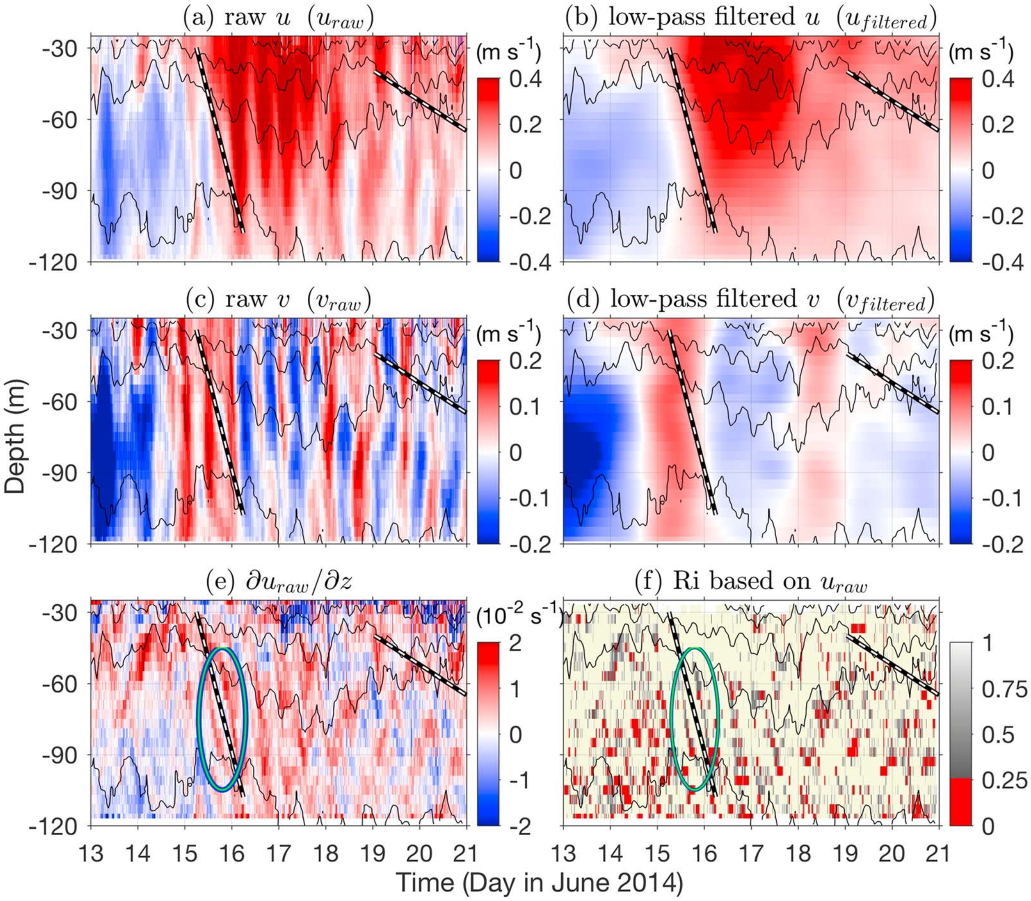

Figure 6. Time series of (left) raw and (right) low-pass filtered (a and b) u, (c and d) v, (e) $\partial u/\partial z$, and (f) Richardson number at the Central Offshore mooring on 13–21 June 2014. The thin black lines are isopycnals with the interval of 0.5 kg/m^3; the white dashed lines corresponding to the descending signals in the mooring temperature and salinity data (Figure 3 right column); the green ellipses in (e) and (f) highlight the region of slightly enhanced mixing.

3.2. Dynamics of the Frontal Filaments

Based on their length and velocity scales, the observed frontal filaments represent a submesoscale process. The unfiltered ring edge velocity U = 0.5–1 m/s; the cross-shelf length scale of the subsurface shelf-water layer $L_c \approx 10$ km; the thickness of the filaments $H \approx 20$ m; $N \approx 0.02$ s^{-1}; and $f = 9.37 \times 10^{-5}$ s^{-1}. Substituting these into (1) and (2) gives Ro = 0.5–1 and Fr = 1–3, both $O(1)$. Substituting the vertical scale of the WCR in the slope sea, H_r = 500 m, into (3) gives the first baroclinic Rossby radius of deformation of the WCR in the slope sea, $L_R \approx 100$ km. Therefore, $L_c < L_R$. All these satisfy the scaling for submesoscale features (McWilliams, 2016). As described in section 1, two mechanisms could potentially form the observed submesoscale frontal filaments: (i) ageostrophic frontal subduction and (ii) horizontal stirring by geostrophic shear flow. Here we discuss the possibility of each process occurring at the ring edge.

Some of the filaments, except the one on 19–21 June at the CO mooring (Figures 3 and 6), appear to be crossing isopycnals, differing from the classical pattern of along-isopycnal frontal subduction (e.g., Spall, 1995). The isopycnals over the filament periods generally move downward but in a pace slower than the apparent filament descent. Consequently, some of the filaments cross the isopycnals, and density (and salinity) increases along the filaments. However, the filaments could still result from frontal subduction, even though their cross-isopycnal characteristics do not fit the classical pattern of frontal subduction. Other frontal processes could act on top of the frontal subduction, modify the pattern, and result in the cross-isopycnal appearance. One potential process is the mixing of the filament shelf water with the surrounding high salinity water. To examine this, we compute time series of the vertical shear of horizontal velocity, $\partial u/\partial z$ and $\partial v/\partial z$, at the CO mooring and the corresponding Richardson number,

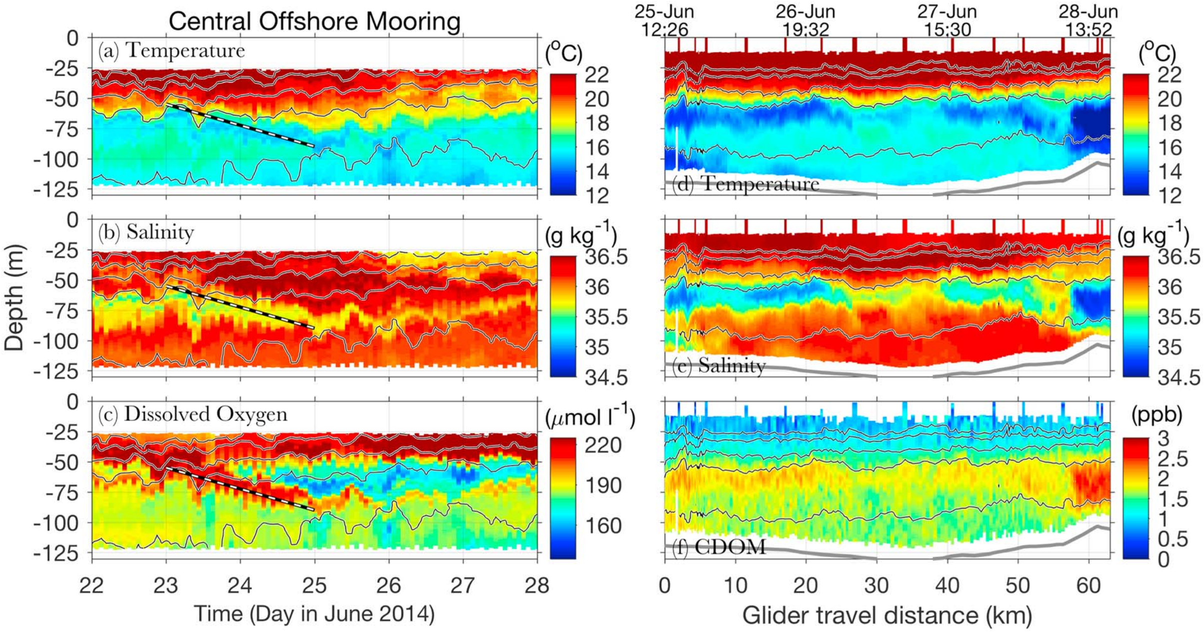

Figure 7. (left) Time series of potential temperature, absolute salinity, and dissolved oxygen measured by the CO mooring over 22–28 June 2014; (right) along-shelf section of temperature, salinity, and colored dissolved organic matter measured by a Pioneer Array FZ glider over 25–28 June 2014 with the track shown in Figure 1d. The thin solid lines in each panel are isopycnals with the contour internal of 0.5 kg/m^3. The dashed lines in the left panels highlight the descending signal. The grey thick lines in (d)-(f) are the bottom. The mooring colored dissolved organic matter and glider dissolved oxygen data are not shown because of bad data.

$$\mathrm{Ri} = \frac{\mathrm{N}^2}{\left(\partial \mathrm{u}/\partial \mathrm{z}\right)^2 + \left(\partial \mathrm{v}/\partial \mathrm{z}\right)^2}. \tag{7}$$

The computation was done with raw u and v (Figures 6e and 6f), and the N is interpolated onto the same vertical 4-m grid as the velocity. It shows two bands of slightly elevated $\partial u/\partial z$, low Ri, and presumably enhanced mixing on the top and bottom faces of the filament on 15–17 June. The enhanced vertical shear may be caused by the tidally induced internal waves in the region. However, the enhancement pattern is not distinct, and it remains unclear whether mixing in the shelfbreak region is strong enough to modify the properties of the filament water and result in the density variation along some of the filaments.

Another potential reason is that the observed filaments represent a subsurface 3-D cross-isopycnal sheet of shelf water being subducted at different isopycnals with different temperature, salinity, DO, and CDOM properties. This may occur because the tracer contours in the MAB shelfbreak region often misalign with the isopycnals owing to the great spiciness caused by the strong density compensation of temperature and salinity (e.g., Todd et al., 2013; Zhang et al., 2011). The 3-D shelf-water sheet could then be advected though the moorings by the eastward frontal current and form the filaments with cross-isopycnal descending appearance (see section 4 for more discussion on this).

Frontal geostrophic shear flow, as the other possibility of generating the tracer filaments, can intensify *existing* horizontal tracer gradients at depth through stirring, as described in (4), and forms a 3-D, cross-isopycnal, tilted tracer sheet (Smith & Ferrari, 2009). However, this purely geostrophic process would not induce vertical motion to transport the near-surface shelf water downward to the depth of the observed filaments. Other downward transport processes are required to establish the initial horizontal tracer gradients. Hence, regardless what causes the cross-isopycnal appearance of the filaments, the data suggests that some type of downwelling motion occurs at the ring edge. However, if the geostrophic shear stirring takes place, the apparent signal descent observed at the moorings would be at least partially caused by the shear distortion, and the speed of the downward motion would be slower than the apparent descend rate.

Despite capturing the frontal filaments, the Pioneer Array measurements are not sufficient to resolve the temporal and spatial gradients associated with the filaments, which prevents the analysis of the submesoscale

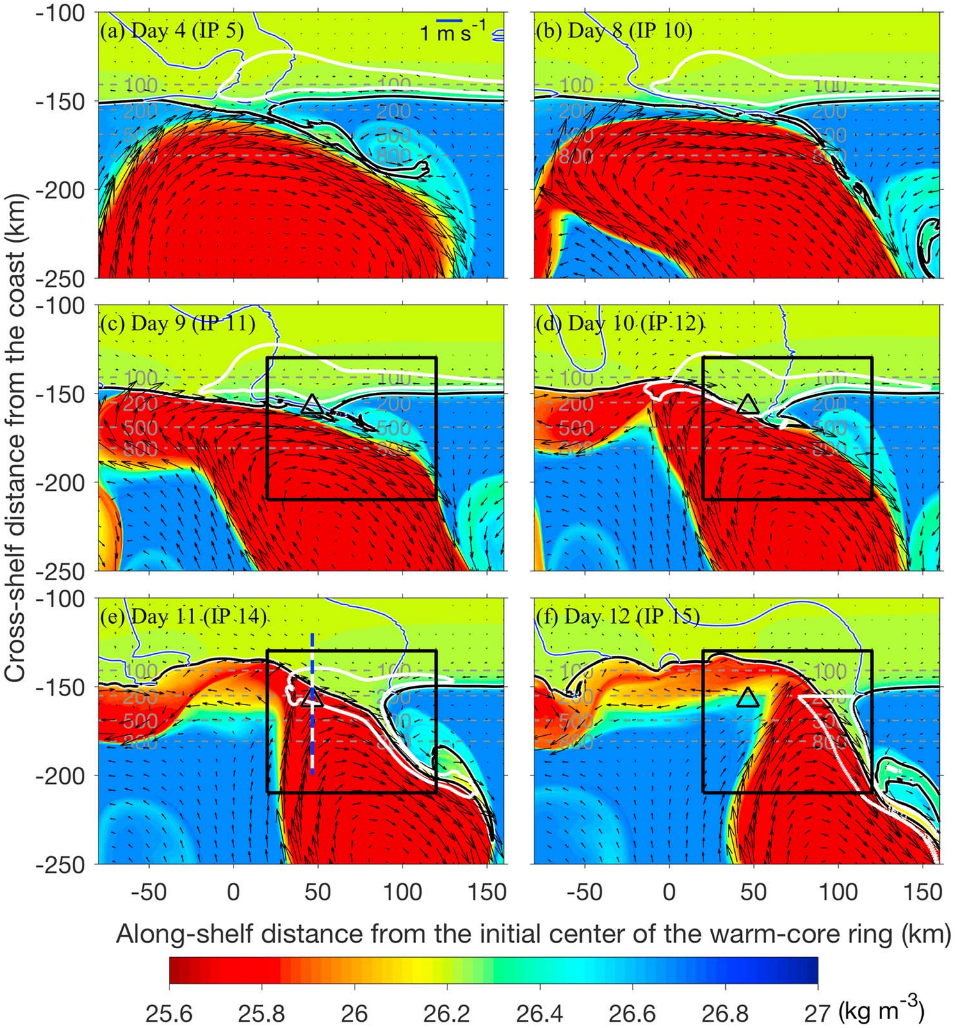

Figure 8. (a–f) Snapshots of the model surface density (color) and velocity (vectors) at different times. The black lines are the contour of 50% shelf water concentration; the thin blue lines are the contours of zero vertically averaged along-shelf current on the shelf, outlining the shelf region under barotropic influence of the ring; the thick white lines depict the source region of the day 12 streamer shelf water at different times obtained from the adjoint simulation; the triangles in (c)–(f) indicate the location of the model time series shown in Figure 9, left column; the blue-white dashed line in (e) indicates the cross-shelf transect shown in Figure 9, right column; the boxes in (d)–(f) depicts the area of view in Figure 10; the grey dashed lines are isobath contours; *IP* in each panel represents inertial period.

dynamics. The distance between the CO and OS moorings is 17.6 km, greater than the filament length scale. The time it takes a glider to cross the frontal region is about 1 day, which is similar to the filament development time scale. There were only one EB glider and one FZ glider in the region in June 2014, and they were over 30 km apart. In order to resolve the submesoscales, we use model simulations to examine the dynamics of the observed frontal filaments.

4. Modeling Analysis

4.1. General Pattern in the Model

SST from the ROMS control simulation shows surface deformation of the WCR (Figure 8) in a pattern qualitatively similar to the structure observed in the satellite images (cf. Figure 1). The ring and shelf waters come in direct contact on Day 9 as a limb of the WCR moving clockwise along the ring periphery reaches the 200-m isobath. At day 10, some shelf water is pulled offshore of the 200-m isobath at $x \approx 50$ km. By day 11, a prominent shelf-water streamer of 5–20 km wide has formed on the northeastern periphery of the WCR, and

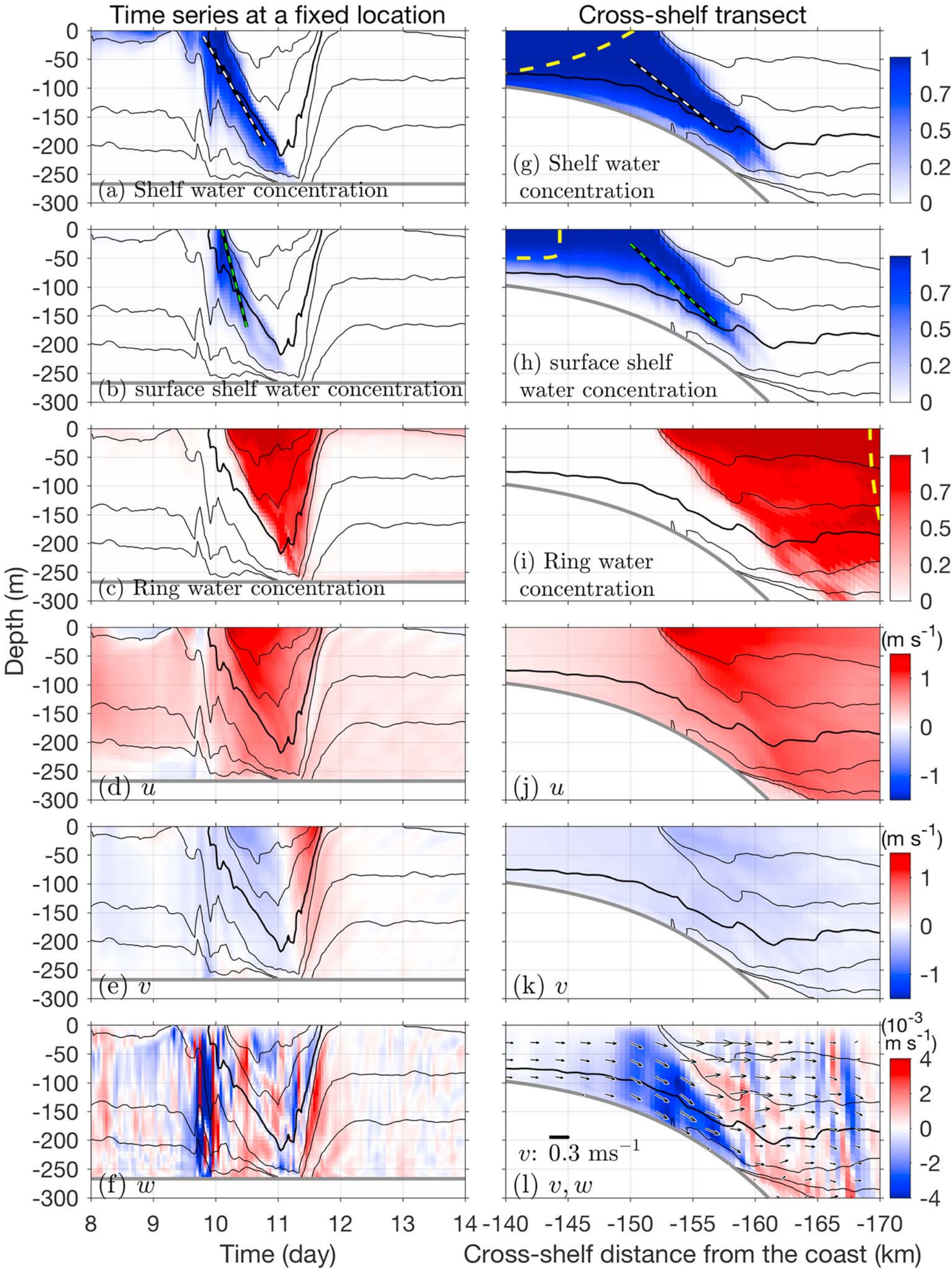

Figure 9. (left) Time series of modeled (a) shelf water concentration (C_s), (b) surface shelf water concentration (C_{s2}), (c) ring water concentration (C_r), (d) eastward velocity, (e) northward velocity, and (f) vertical velocity at a fixed location (triangles in Figures 8c–8f) over the period of frontal subduction; (right) a cross-frontal transect of the same variables at $x = 47$ km and $t = 11$ days (blue dashed line in Figure 8e). The black curves in all panels are contours of σ_θ with the interval of 0.2 kg/m^3 and the 26.3 kg/m^3 contour highlighted in bold. The dashed white lines in (a) and (g) highlight the subduction signals of the shelf water; the dashed green lines in (b) and (h) highlight the subduction signals of the surface shelf water; the dashed yellow lines in (g)–(i) represent the edges of the shelf, surface-shelf, and ring waters, respectively, in the initial conditions.

a cyclonic shelf-water ringlet is developed at the southeast end of the streamer, similar to observations (cf. Figure 1d; Kennelly et al., 1985).

The model resolves the shelf-water frontal filaments at the northern ring edge with a pattern similar to the observed. The left column of Figure 9 shows time series of various water-column properties at a fixed site near the ring-shelf water interface (triangles in Figures 8c–8f), which is comparable to the mooring data. It depicts clear descending signals of the shelf water tracer (C_s; Figure 9a) and surface shelf water tracer (C_{s2}; Figure 9b) at day 10. The signals of both C_s and C_{s2} reaches $z = -220$ m on day 11, much deeper than their respective initial depth range of $z > -80$ m and -50 m (Figure 2). This thus indicates subduction of the shelf water at the ring edge.

The descending filaments of C_s and C_{s2} also differ from each other: the former is mostly along-isopycnal, and the latter is steeper and crosses the isopycnal $\sigma_\theta = 26.3$ kg/m^3 between $z = -100$ and -150 m (Figures 9a and 9b). The former suggests that the subduction occurs within the same isopycnal interval, consistent with the classical pattern of frontal subduction. The cross-isopycnal appearance of the C_{s2} filament resembles some of the mooring-observed filaments. Note that the descending signal of C_s spans a isopycnal range of $\sigma_\theta = 26.1$–26.5 kg/m^3 (Figure 9a) and that C_s has no initial along-isopycnal variation while C_{s2} does with the initial boundary intercepting the isopycnal $\sigma_\theta = 26.3$ kg/m^3 (Figure 2). The difference in the descending signals of C_s and C_{s2} thus suggests that the cross-isopycnal appearance of the descending filament results from (i) subduction transporting C_{s2}, including its cross-isopycnal boundary, in the isopycnal range of 26.1–26.5 kg/m^3 downward forming a 3-D subsurface tracer layer, and (ii) the advection of the 3-D tracer layer passing through the *mooring* generating the cross-isopycnal appearance of the descending filament. Meanwhile, geostrophic shear stirring likely strains the subsurface tracer layer and deforms the tracer boundary. This process could occur in the real ocean as the density compensation between the temperature and salinity in the MAB shelfbreak region causes temperature and salinity contours to intercept the density contours with great spiciness (e.g., Todd et al., 2013). Because the model has no tidally induced internal waves to enhance mixing as in the real ocean, this explanation does not necessarily preclude the possibilities of mixing contributing to the cross-isopycnal appearance of observed filaments. As this study focuses on demonstrating the occurrence of the frontal subduction, the detailed influence of these other factors on the subduction is not investigated here.

Vertical cross-shelf section of the model field at day 11 shows that the initial retrograde shelfbreak front (Figure 2b) has been replaced by a prograde ring-edge front with a clear subduction feature (Figure 9 right), similar to the EB glider observations (Figure 4). In particular, an intermediate layer of shelf water resides underneath a surface of ring water and a bottom layer of slope water. The shelf water is thus not in direct contact with the bottom as it moves offshore, which is also consistent with the observations (e.g., Figure 7). The head of the shelf-water layer has moved offshore by 10 km and downward by 170 m. Cross-shelf section of the model velocity also shows a clear pattern of the subduction flow with offshore and downward velocity (Figures 9k–9l).

The model also shows that the subduction occurs over an along-shelf distance of several tens of kilometers. The vertically integrated C_s shows a substantial amount of shelf water underneath a surface layer of ring water on Day 10–12 (the blue area southwest of the green lines in Figures 10b–10d). On day 10 the subduction layer spans an along-shelf distance of about 60 km, from $x = 0$ to 63 km, and the along-shelf span expands to $>$100 km on day 11.

4.2. Subduction Dynamics in the Model

The modeled ring edge velocity $U \approx 1$ m/s; the cross-shelf and vertical length scales of the subsurface shelf-water layer are $L_c \approx 10$ km and $H \approx 50$ m, respectively; $N \approx 0.01$ s^{-1}; and $f = 9.37 \times 10^{-5}$ s^{-1}. These together give $Ro \approx 1$ and $Fr \approx 2$, both order-one. The modeled subduction feature is thus also a submesoscale phenomenon. To investigate the subduction dynamics, we calculate the divergence (δ), relative vorticity (ζ), stretch-strain deformation rate (S) of the modeled horizontal velocity, and the axial direction of the frontal principal flow deformation. We also perform the frontal tendency diagnosis following Capet et al. (2008a, 2008b) and Gula et al. (2014). The divergence, relative vorticity, and stretch-strain rate are defined as

$$\delta = \frac{\partial u}{\partial x} + \frac{\partial v}{\partial y}, \tag{8}$$

$$\zeta = -\frac{\partial u}{\partial y} + \frac{\partial v}{\partial x}, \tag{9}$$

and

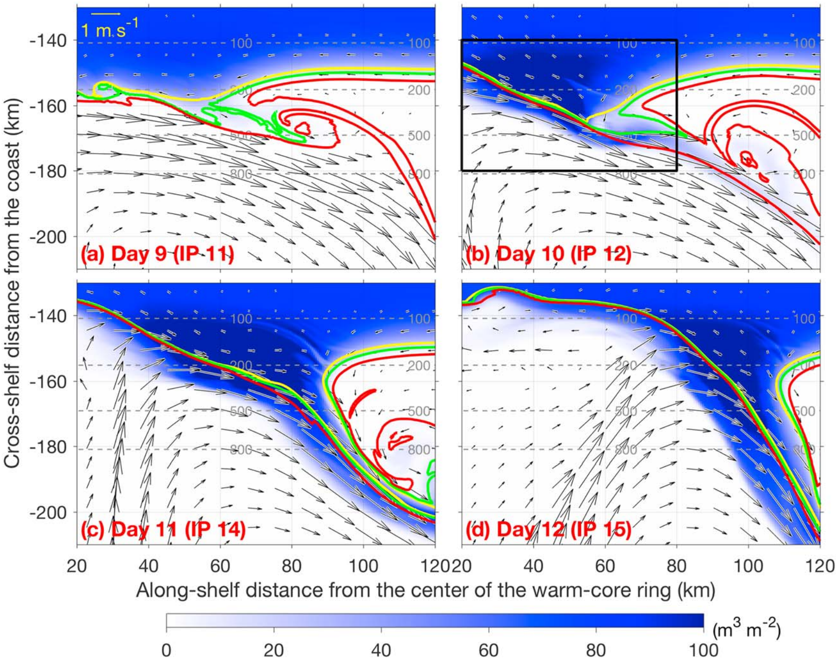

Figure 10. Snapshots of vertically integrated shelf water concentration (i.e., the effective thickness of the shelf water; color) and contours of shelf water concentration C_s = 0.1 (red lines), 0.5 (green lines), and 0.75 (yellow lines) on sea surface. The vectors indicate the surface velocity with the scale at the top-left corner of (a), and the grey dashed lines are isobath contours. The box in (b) indicate the area of view in Figure 11.

$$S = \left[\left(\frac{\partial u}{\partial x} - \frac{\partial v}{\partial y}\right)^2 + \left(\frac{\partial v}{\partial x} + \frac{\partial u}{\partial y}\right)^2\right]^{1/2}, \tag{10}$$

respectively. Note that (10) describes flow deformation due to both stretching and straining (Hoskins, 1982). The direction of the principal flow deformation axis is described by the angle

$$\theta_p = \frac{1}{2}\tan^{-1}\left[\frac{(\partial v/\partial x) + (\partial u/\partial y)}{(\partial u/\partial x) - (\partial v/\partial y)}\right]. \tag{11}$$

The flow deformation is frontogenetic when the principal deformation axis aligns with the frontal axis; that is, the angle between the two axes is $<\pi/4$ (Gula et al., 2014). The frontal tendency, T, is defined as the rate of change of the amplitude of the buoyancy gradient following a fluid parcel and satisfies,

$$T = \frac{1}{2}\frac{D\|\nabla b\|^2}{Dt} = T_{\mathrm{adv}} + T_w + T_{\mathrm{dv}} + T_{\mathrm{dh}}, \tag{12}$$

where,

$$T_{\mathrm{adv}} = \left(-\frac{\partial b}{\partial x}\nabla_h u - \frac{\partial b}{\partial y}\nabla_h v\right)\cdot\nabla_h b, \tag{13}$$

$$T_w = -\frac{\partial b}{\partial z}\nabla_h w\cdot\nabla_h b, \tag{14}$$

and

$$T_{\mathrm{dv}} = \nabla_h\left[\frac{\partial}{\partial z}\left(\kappa_\theta\frac{\partial b}{\partial z}\right)\right]w\cdot\nabla_h b \tag{15}$$

are the contributions of horizontal advection, vertical advection, and vertical mixing to the frontogenesis, respectively; and T_{dh} is the effect of the horizontal diffusion, which is implicit within the model numerical advection scheme in this study. In (12)–(15), $b = -g(\rho/\rho_0)$ is buoyancy, w is vertical velocity, κ_θ is vertical turbulent diffusivity, and $\nabla_h = (\partial x, \partial y, 0)$. A positive (negative) value of the right-hand-side terms in (12) means the corresponding process is frontogenetic (frontolytic). T_{dh} is always frontolytic because the numerical diffusion tends to smear the horizontal density gradient. As in Gula et al. (2014), T_{dh} is generally secondary and thus neglected here.

The diagnostic quantities at $z = -3$ m and $t = 10$ days (Figure 11) shows a peak of front sharpness on the ring-shelf water interface west of $x = 63$ km with prominently downward velocity, convergence (negative divergence), positive vorticity, and large stretch-strain rate. The principal deformation axis generally aligns with the axis of the front. These are all characteristics of frontogenesis. The ring-shelf water interface east of $x = 63$ km does not show a clear signal of frontogenesis. The frontal tendency diagnosis shows that the horizontal flow advection strengthens the front in the region of frontogenesis, while the vertical advection weakens the front. The effect of the vertical mixing on the frontal strength is negative at the core of the front and positive to the immediate southwest of the front.

A cross-front vertical section of the diagnostic quantities at day 10 (Figure 12) shows that the frontogenesis pattern persists at depth. A stripe of elevated frontal sharpness, convergence, positive relative vorticity, and strong flow deformation aligns with the ring-shelf water interface (the region of closely spaced black and grey lines in Figure 12). The frontal tendency diagnosis shows that effects of horizontal and vertical advection at the front are positive and negative, respectively, and tends to balance each. The influence of vertical mixing is negligible below the surface. These are all consistent with the frontogenesis dynamics of filaments (double-sided fronts) in the Gulf Stream (Gula et al., 2014). The cross-shelf alternating positive and negative vertical velocities onshore of the front (Figure 12d) and undulations of the isopycnals and C_s contour reflect high-frequency internal waves excited at the front propagating onshore. Close examination of the model solution indicates that these internal waves are generated by the rapid onshore migration of the northern ring edge.

A region of negative vertical velocity of ~5 km wide and 100 m thick is visible below the ring-shelf water interface and offshore of $x = 0$ (inside the black frame in Figure 12d). It reflects the subduction flow and generates the downward extending tongue of the shelf water. A zoom-in view of the vertical and cross-frontal velocity in this frontal zone show the subduction as a part of the cross-front secondary flow induced by the frontogenesis (Figure 13): An upwelling flow on the offshore side of the front transitions to an onshore cross-frontal flow on the surface and then a downwelling flow on the onshore side of the front.

All these confirm the occurrence of the 3-D front subduction of the shelf water on the onshore edge of the WCR. Essentially, as depicted in Figure 14 schematically, the WCR impinges on the shelf edge, and the cross-shelf density gradients on the onshore edge of the ring intensify. This frontogenesis causes flow straining and induces an ageostrophic cross-front secondary circulation with strong vertical motion through potential vorticity conservation (e.g., Capet et al., 2008a; Hoskins, 1982; McWilliams et al., 2009; Spall, 1995). Specifically, intensification of the frontal density gradient strengthens the frontal jet and also vorticity on both sides of the jet (more negative on the light side and more positive on the heavy side). Potential vorticity conservation then drives upwelling on the light side of the front and downwelling on the heavy side of the front. An ageostrophic cross-frontal surface flow from the light side toward the heavy side and a subsurface compensating flow in the opposite direction develop. This secondary flow tends to relax the steepening front. The downwelling velocity on the heavy side of the front and the subsurface compensating flow together form the frontal subduction (Spall, 1995). The subducted water is then carried along the ring periphery away from the subduction site by the frontal current, while the frontal subduction continues taking place on the onshore ring edge as the ring keeps impinging on the shelf edge. The along-front extent of the subduction is consistent with the along-front extent of frontogenesis, which is controlled by the background convergent flow.

Close examination of the model solution show that this subduction process actually occurs on the ring-slope water interface before the ring water is in contact with the shelf water (Figure 8a). That is, as the WCR starts to impinge on the shelf edge and the ring edge front starts to intensify, the slope water that initially resides between the ring and shelf waters is subducted and carried away. As the ring edge continues moving shoreward, it comes into contact with the shelf water. Because the surface ring water is less dense than the shelf

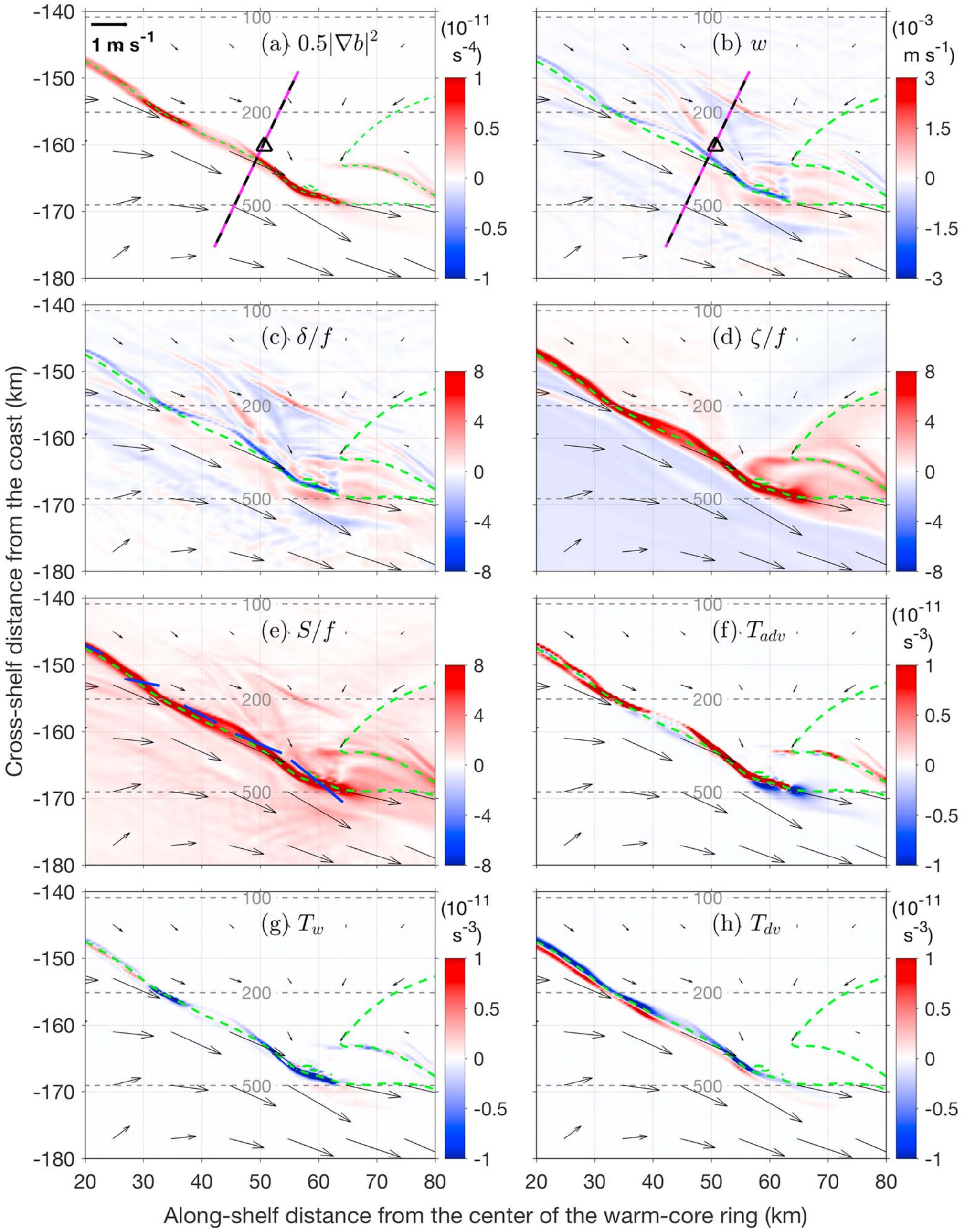

Figure 11. Horizontal distribution of (a) frontal sharpness, (b) vertical velocity, (c) divergence, (d) relative vorticity, (e) stretch-strain rate (color), and principal deformation axis (thick blue lines), as well as the frontogenesis tendency terms due to (f) horizontal advection, (g) vertical advection, and (h) vertical mixing at $z = -3$ m and $t = 10$ days in a frontal region (black box in Figure 10b). The dashed green lines are the contour of C_s $(x, y, 0) = 0.5$, indicating the location of the ring-edge front; the arrows are vectors of the surface velocity; the triangles in (a) and (b) indicate the location of the model time series in Figure 9, left column; the dashed black-magenta lines in (a) and (b) indicate the location of the cross-frontal section in Figure 12; the grey dashed lines are isobath contours.

water, the ring-edge density front persists, and the subduction now transports the shelf water downward. The ring edge current then carries the subducted shelf water into the slope sea. During this process, the initially retrograde front at the shelf break is destroyed and replaced by the prograde density front, as indicated by the orientation change of the isopycnals at 150-m water depth ($y = -150$ km) from Figures 2b to 9g. Meanwhile, the surface cross-shelf density gradient, $\partial\rho/\partial y$, at $y = -150$ km has changed from its initial value of -0.6×10^{-4} kg/m^4 to 6×10^{-4} kg/m^4.

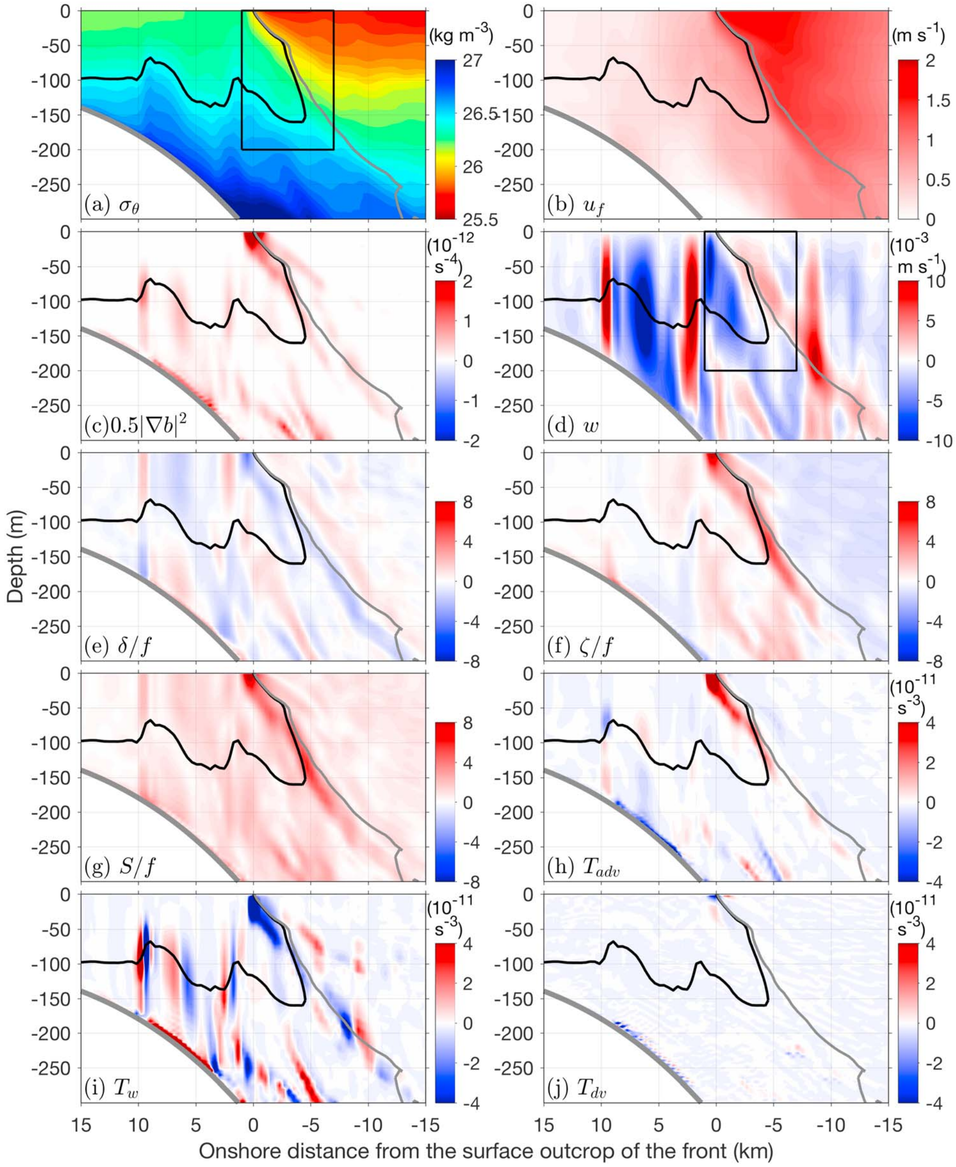

Figure 12. Cross-frontal section of (a) σ_θ, (b) eastward velocity, (c) frontal sharpness, (d) vertical velocity, (e) divergence, (f) relative vorticity, (g) stretch-strain rate, and the frontogenesis tendency terms due to (h) horizontal advection, (i) vertical advection, and (j) vertical mixing along a line normal to the front (magenta lines in Figures 11a and 11b) at $t = 10$ days. The black lines are the contours of $C_s = 0.5$, and the grey lines are the contours of $C_r = 0.5$. The boxes in (a) and (d) indicate the zoom-in region shown in Figure 13.

5. Discussion

5.1. Subduction Transport of the Shelf Water

The model shows that the subducted shelf water underneath the surface ring water is eventually transported offshore, providing a process of cross-shelfbreak offshore transport of the shelf water that has no surface expression. The model demonstrates that this subsurface transport of the shelf water occurs alongside of the surface-visible (to satellites) shelf-water streamer (Figure 10). This is consistent with field observations sometimes showing subsurface shelf water adjacent to *surface-visible* shelf-water streamers on the periphery of WCRs (e.g., Kupferman & Garfield, 1977; Tang et al., 1985). From the prospective of someone who analyzes satellite remote-sensing data, the subsurface offshore transport of the subducted shelf water thus behaves as a *surface-invisible* part of the streamer transport.

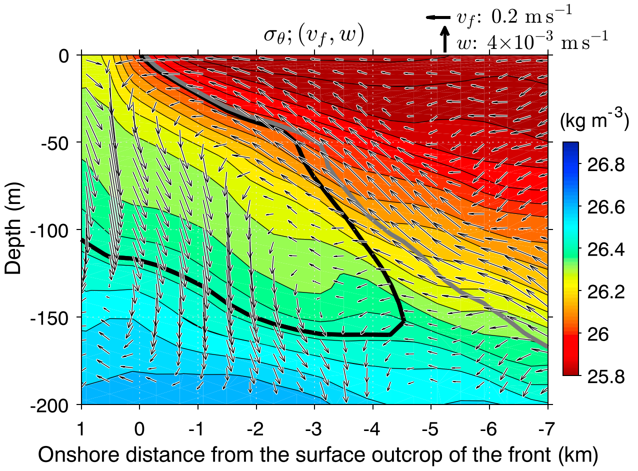

Figure 13. A zoom-in view of the density (color) and secondary circulation (v_f and w; vectors) on the cross-frontal section (see the boxes in Figures 12a and 12d for the area of view). Here v_f is horizontal velocity in the cross-frontal direction. The scales of v_f and w are shown on the top-right corner. The black and grey lines are the contours of the shelf and ring water concentration of 0.5, respectively.

Here we seek to qualitatively estimate the subduction-associated subsurface cross-shelfbreak offshore transport (referred to as *surface-invisible*) of the shelf water in the model and compare it to the *surface-visible* streamer transport. This separation is for a practical purpose. As satellite data are often used to illustrate the shelf-water streamer in the literature with an implicit assumption that the streamer transport is all visible on the surface, quantifying the surface-invisible part of the shelf water transport reveals the amount of cross-shelfbreak offshore transport that is missed if one is to estimate the overall transport based only on the surface information and some scaled depth (e.g., Bisagni, 1983) or using a low-resolution model that does not resolve the subduction process (e.g., Chen et al., 2014). To our knowledge, the surface-invisible offshore transport of the shelf water has not been specifically quantified in the literature, even though it is included in the overall streamer transport of the shelf water in some studies (e.g., Cherian & Brink, 2016).

Because the rapid evolution of the ring-shelf water interface hampers a direct calculation of the shelf-water transport, we compute the transport indirectly from the temporal change of the surface-visible and -invisible shelf water volume in the slope sea (offshore of the 200-m isobath). The total volume of shelf water in the slope sea at time t is computed using the shelf water passive tracer concentration, C_s; that is,

$$P_t(t) = \iiint_{V_{\mathrm{offshore}}} C_s(t)\,dxdydz, \tag{16}$$

where V_{offshore} is the entire model volume offshore of the 200-m isobath. The separation of the surface-visible and -invisible portions is based on the surface shelf-water concentration, $C_s(x, y, 0)$. If $C_s(x, y, 0) > 0.1$, all shelf water within the water column underneath $(x, y, 0)$ is considered surface-visible, and its domain-integrated volume in the slope sea, P_v, is assumed to be the volume of shelf water that has been transported offshore in the surface-visible streamer. The rest of the shelf water in the slope sea is considered surface-invisible and has been transported offshore by the entrainment process associated with the frontal subduction. Its domain-integrated volume in the slope sea is $P_i = P_t - P_v$. The time rates of change of the volume quantities, $Q_t = \partial P_t/\partial t$, $Q_v = \partial P_v/\partial t$, and $Q_i = \partial P_i/\partial t$, are calculated as the total, surface-visible, and surface-invisible cross-shelfbreak offshore transport of shelf water, respectively. Note that this approach assumes (i) only one continuous vertical layer of shelf water in the water column and (ii) no exchange of the two categories occurring offshore. It is very likely that these assumptions do not hold in the real ocean, especially after a relatively long-period evolution of the streamer in the slope sea. However, as this work focuses on the first several days of the streamer evolution and the goal here is to provide a qualitative sense on the baroclinic transport, the issues are not expected to severely affect the result.

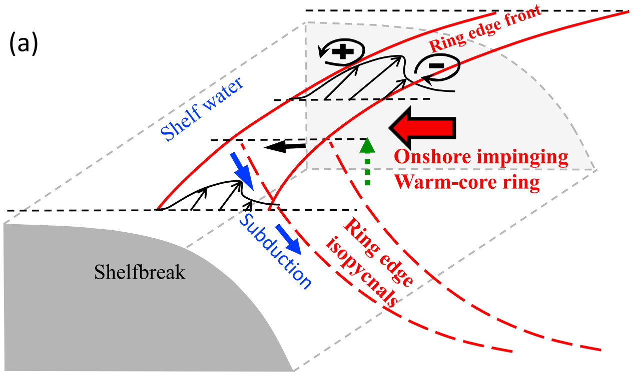

Figure 14. A schematic of the 3-D frontal subduction processes at the northern edge of the impinging warm-core ring. The big red arrow indicates the onshore migration of the WCR; the solid red lines represent two ring-edge isopycnals on the surface; the dashed red lines represent two ring-edge isopycnals on the vertical cross-shelf section; the thin black arrows represent the frontal jet on the surface. The blue, thick black, and dashed green arrows depicts the secondary flow on a cross-frontal vertical section: The solid blue arrow indicates the subduction flow on the heavy side of the front; the thick black arrow indicates the cross-frontal onshore flow on the surface; the dashed green arrow indicates the upward flow on the light side of the front.

Applying the separation approach to the control simulations shows that P_t, P_i, and P_v all increase over time in the 20-day simulation period (Figure 15a). P_v starts to increase slowly at day 5, earlier than P_i. It is consistent with the shelf-water streamer developing ahead of the shelf-water subduction (Figure 10). Starting from Day 9, P_i starts to increase rapidly and catches up with P_v at day 14. After that, P_i saturates, while P_v continues increasing. The saturation of P_i is caused by the cease of the frontogenesis and subduction process as the ring limb (pointing northward in Figure 8f) leaves the shallow region. Overall, P_i and P_v are of the same order of magnitude. Correspondingly, Q_i increases dramatically starting from day 9 and reaches a peak of 0.8 Sv on day 12, representing 90% of the overall shelf-water cross-shelfbreak offshore transport at the time (red lines in

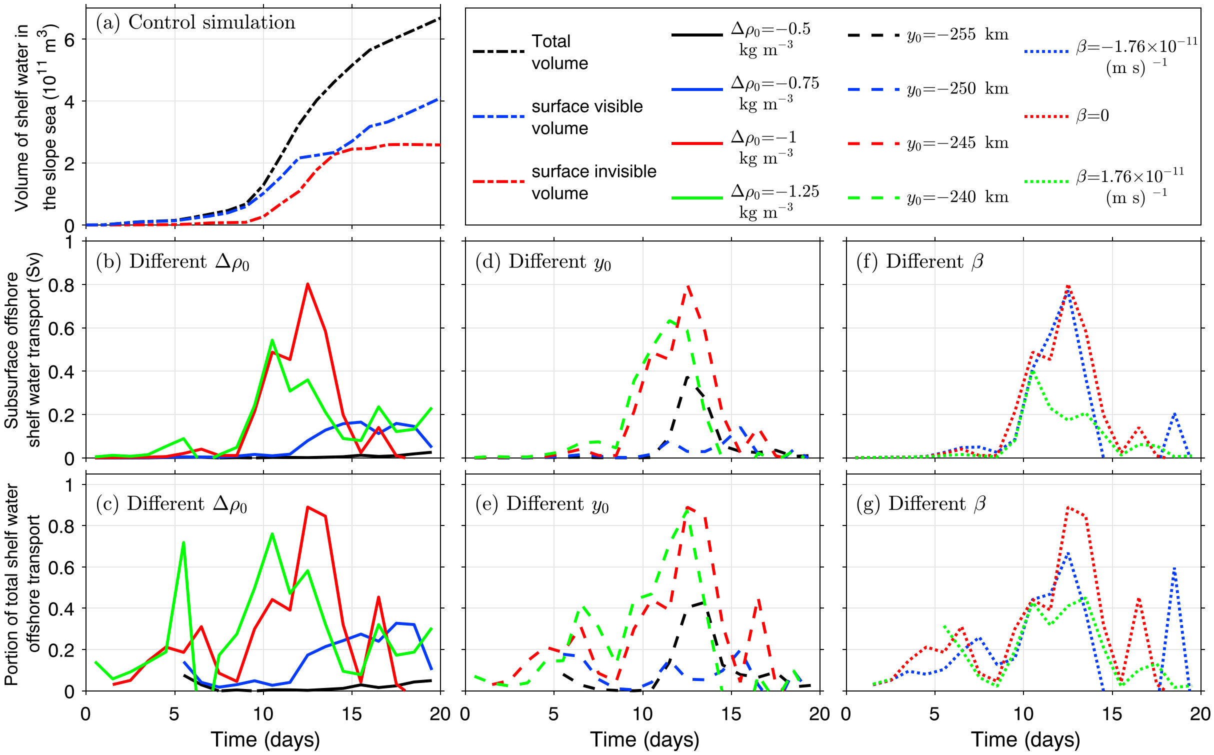

Figure 15. Time series of modeled (a) volume of shelf water in the slope sea (offshore of the 200-m isobath), (b, d, and f) surface-invisible offshore transport of the shelf water, and (c, e, and g) fraction of the total offshore shelf water transport being surface invisible. The results in (a) are obtained from the control simulation, those in (b) and (c) are from sensitivity simulations of different ring water density anomaly ($\Delta\rho_0$), those in (d)–(e) are from sensitivity simulations of different initial cross-shelf position of the ring (y_0), and those in (f)–(g) are from sensitivity simulations of different β. The red curves in (b)–(g) are obtained from the control simulation. In (c), (e), and (g) only the faction at times of the total offshore shelf water transport exceeding 0.02 Sv is shown.

Figures 15b and 15c). Over the 7-day period (days 9–15) of shelf-water frontal subduction, the mean surface-invisible offshore transport of the shelf water is ~0.4 Sv. It is thus possible for the shelf-water offshore transport induced by the frontal subduction to be a substantial transport relative to other mechanisms (e.g., PNI and surface visible streamers).

Analysis of the satellite data over the period of 1979–1985 showed that WCR-associated shelf-water streamers were present in the MAB region for ~70% of the time (Garfield & Evans, 1987). Assuming the subduction-induced subsurface transport occurs over 1/4 of those times and all subduction events induce the shelf-water transport of 0.4 Sv, the same as in our control simulation, the surface-invisible offshore transport of the shelf water averaged over all times would be ~0.07 Sv. This is significant relative to the shelf-water offshore transport of 0.04–0.11 Sv required to balance the entire MAB volume budget (Brink, 1998). However, this is likely an overestimate as the simulations presented in this study are based on a highly idealized model configuration of one particular scenario. A more precise estimate of the subduction-induced shelf-water offshore transport would require observations of higher spatial and temporal resolution or realistic model simulations.

We here examine the dependence of modeled Q_i on the density anomaly of the ring water ($\Delta\rho_0$, which is related to the strength of the ring), the initial cross-shelf location of the WCR (y_0), and the spatial variation of f (Table 1). The simulations of different $\Delta\rho_0$ show that when $|\Delta\rho_0| \leq 1$ kg/m^3 Q_i increases with $|\Delta\rho_0|$ (Figure 15b), suggesting that intensity of the frontal subduction increases with the strength of the ring-edge front. But, as$|\Delta\rho_0|$increases from 1 to 1.25 kg/m^3, Q_i decreases slightly. The simulations of different y_0 show that the subduction generally intensifies as the WCR gets closer to the shelf break (Figures 15d and 15e). The simulations with spatially varying f (β-plane) show that the cross-shelf migration of the WCR resulted from the β-effect (Early et al., 2011) affects the subduction process (Figures 15f and 15g). However, the relationships of Q_i with $\Delta\rho_0$, y_0, and f are not linear. Closer examination of the model solutions shows that the subduction intensity depends highly on the specific shape of the interface between the ring and shelf waters. The ring-shelf water interface is strongly affected by the finite-amplitude instability on the ring periphery. The $\Delta\rho_0$, y_0, and f all exert strong influences on the instability on the ring periphery. These influences and the development of the finite-amplitude ring-edge instability are all nonlinear and might be related to the cross-frontal difference in the potential vorticity. The detailed relationships between the subduction process and those influencing factors and the underlying dynamics are left for future studies.

5.2. Comparison With the Open Ocean Process

The basic dynamics of the frontal subduction described here is the same as the submesoscale frontal processes previously studied in the open ocean environment. Essentially, the frontal subduction is part of the cross-front secondary circulation that tends to flatten the steepening front.

A major difference between the shelfbreak environment and the open ocean is the presence of the shallow sloping bottom. It exerts strong influence on the evolution of the WCR (e.g., Cherian & Brink, 2016, 2018) and presumably causes the background confluence flow on the ring edge that drives the frontal subduction. For the barotropic offshore flow of the shelf water, the vertical stretching associated with the sloping bottom is also important for the vorticity dynamics (Cherian & Brink, 2018). However, the subducted shelf water is separated from the bottom by a bottom layer of slope water (Figures 4 and 9), and the subduction layer of 20–50 m thick is relatively thin compared to the water column of 100–200 m thick. Its dynamical evolution is thus less likely influenced directly or altered qualitatively by the sloping bottom.

Because the MAB shelf break separates the shelf and slope/ring waters of dramatically different physical and biogeochemical, the shelfbreak subduction process, as a part of the cross-shelf transport, is potentially important. It could greatly affect the heat and salt balance on the shelf and export the outer shelf water that is rich in organic matter into the deep part of the open ocean. The temperature and salinity differences between the adjacent shelf and ring waters can reach 18°C and 3.5 g/kg (Zhang & Gawarkiewicz, 2015a). Meanwhile, density difference between the waters is generally <1 kg/m^3, as much of the density effects of temperature and salinity are compensatory. As demonstrated in section 3, the dramatic differences in the water properties provide a great opportunity for visualizing the frontal subduction. The differences of the water properties across a front in the open ocean are likely smaller, and the signal of frontal subduction there is likely less visually dramatic.

5.3. Potential Implication on Dynamics of Shelf-Water Streamer

The potential influence of the frontal subduction on the shelf-water streamer is considered here. We pose the hypothesis that the frontal subduction facilitates the entrainment of the shelf water by the WCR and enhances the offshore streamer transport of the shelf water.

The shelf-water subduction occurs on the shore side of the ring-edge front and replaces the initially flat or retrograde isopycnals within a 5- to 10-km wide region next to the ring-edge front with prograde isopycnals (Figures 9g–9l and 12a). Frontal subduction thus spreads the prograde ring-edge front shoreward into the shelf water. This is consistent with the EB glider transects showing the change of the shelf-water isopycnals at the 100-m isobath from a retrograde tilt in the end of May before the ring impingement (not shown) to a prograde tilt on 2–3 June after the ring impingement (Figures 4a and 4b). Note that the onshore edge of the ring has not yet reached the 100-m isobath on 2–3 June. Through the thermal-wind balance, the prograde shelf-water isopycnals on 2–3 June presumably enhances the eastward flow of the shelf water. This essentially represents a baroclinically enhanced entrainment of the shelf water by the ring-edge current in a narrow region at the outskirt of the ring edge. Presumably, the same baroclinic mechanism applies to the ring edge to the eastern end of the ring-shelf contact region where the baroclinically entrained shelf water would flow southeastward into the streamer. The thermal-wind enhancement of the shelf-water entrainment by the prograde front is consistent with the weaker cross-shelfbreak subsurface transport of the shelf water in the sensitivity simulation of$|\Delta\rho_0| = 0.75$ kg m^{-3} (Figure 15b). Compared to the control case, the initial shelfbreak front in that case is weaker with smaller density difference between the shelf and ring waters. Consequently, the prograde front at the later stage is weaker, which further weakens the subsurface offshore transport of the shelf water.

This subsurface baroclinic enhancement process is not included in the barotropic mechanism of streamer formation proposed by Cherian and Brink (2016, 2018). Without the shelf break front, their model shows that the outward sea level setdown of the ring spreads onto the shelf as a barotropic influence and drives a geostrophic flow of the shelf water. This barotropic shelf flow is ~40 km wide for the MAB scenario and named shelf-water supply jet as it carries the shelf water along the ring periphery and into the slope sea forming the shelf water streamer. The control simulation here shows a region of 30–60-km wide north of the ring edge (enclosed by the blue contours in Figure 8) where the depth-averaged velocity changes from initially westward to eastward as the ring impinges onto the shelf edge. This region presumably reflects the barotropic influence of the ring on the shelf and corresponds to the barotropic shelf-water supply jet. Thus, in this model the subduction-associated baroclinic transport takes place at the same time as the barotropic transport and presumably enhances the cross-shelfbreak offshore transport of the shelf water into the streamer. The baroclinic transport occurs over a region of only 5–10 km wide, much narrower than the shelf region under the barotropic influence of the ring, and is thus a part of the large-scale barotropic transport of the combined ring, slope, and shelf water on the upper-slope and outer-shelf.

To examine the temporal evolution of the streamer water volume before the formation of the streamer, we use an adjoint tracer model (Zhang et al., 2010) starting from the 3-D volume of the streamer on day 12 (the white contour in Figure 8f). The model simulates the backward tracer advection and diffusion of the shelf water. The adjoint shelf-water tracer is then vertically integrated to obtain the shelf-water thickness at each location and time. The 10-m thickness contours are used to outline the locations of the streamer shelf water at the earlier times, i.e., the source regions (the white lines in Figures 8a–8e). The result depicts the concurrence of the subduction-associated subsurface transport and the surface-visible barotropic transport of the shelf water.

However, it remains unclear how the subduction-associated baroclinic process would dynamically interact with the barotropic process and whether it is a separate mechanism of forming the shelf-water streamer or merely an enhancement to the barotropic mechanism. Another related question is where the streamer shelf water originates on the shelf. The adjoint simulation indicates that, in this particular scenario with the shelfbreak front, the streamer shelf water come from both east and west sides of the streamer. However, whether this is generally true is a question to be explored in future studies.

6. Summary

This study investigates the subduction of the MAB shelf water on the northern edge of an impinging WCR as an enhancement to the transport of the shelf water into the slope sea. This form of subduction-induced offshore transport of the shelf water at the shelf break occurs below the surface and does not have surface signature. It explains historical observations of subsurface packets of shelf water in the slope sea along the ring periphery whose formation mechanism was not specified in the literature.

Analysis of the satellite and OOI Pioneer Array observations in the shelf break region as well as an idealized numerical model simulation shows that the shelf-water subduction is associated with the onshore impingement of the WCR and occurs when the ring and shelf waters are in direct contact. Observations by the Pioneer Array moored profilers in June 2014 show episodic filaments of diluted shelf water appearing descending downward reaching depth beyond the normal depth range of shelf water. The downward signal propagation coincides with the northern edge front of the WCR moving through the moorings. A glider cross-shelf transect through the ring edge show a layer of shelf water locating underneath the ring water. The model simulation reproduces the basic pattern of shelf water subduction on the northern edge of an idealized WCR.

Both the Rossby and Froude numbers of the observed and modeled subduction are order-one, meaning that the subduction is a submesoscale process, same as the frontal subduction in the open ocean environment. Similar to the open ocean process, the shelfbreak subduction on the northern edge of the WCR results from frontogenesis and is a part of the cross-front secondary circulation that tends to relax the intensifying density front. The subduction is a downwelling flow on the onshore side of the ring-edge front and entrains the shelf water into the frontal region. The frontal current then carries the subducted shelf water offshore underneath the ring water. Dynamics of the WCR-induced shelf-water frontal subduction at the shelf break is the same as the frontal subduction in the open ocean. However, the dramatically different physical and biogeochemical properties of the shelf and ring waters at the shelf break provide a great opportunity to visualize the subduction process.

The model also shows that the subducted shelf water is transported offshore alongside of the surface-visible (to satellites) shelf water streamer. This strong connection means that the subduction-induced subsurface cross-shelfbreak offshore transport of the shelf water may be considered as a part of the shelf-water streamer. The model shows that the surface-invisible offshore transport of the shelf water can be substantial relative to the surface-visible streamer transport. The sensitivity simulations indicate that the subduction-induced subsurface offshore transport of the shelf water varies strongly with the density anomaly of the ring water, cross-shelf position of the ring, and spatial variation of the Coriolis parameter. To quantify the subsurface transport of the shelf water associated with a particular WCR impingement event would require observations of much higher spatial and temporal resolution or realistic high-resolution model simulations.

We also propose that the frontogenesis-associated frontal subduction facilitates the formation of the shelf-water streamer along the WCR periphery. The subduction-associated downward flow results in onshore spreading of the prograde ring-edge density front in a narrow region on the outskirt of the ring edge, which then enhances the barotropic along-frontal flow of the shelf water in the region. This process likely contributes to the entrainment of shelf water by the WCR and the formation of the shelf-water streamer. How this baroclinic process interacts with the barotropic transport remains to be investigated.

Acknowledgments

W. G. Z. was supported by the National Science Foundation under grants OCE-1657853, OCE-1657803, and OCE 1634965. JP is grateful for the support of the Woods Hole Oceanographic Institution Summer Student Fellow Program in 2016 and 2017. W. G. Z. thanks Kenneth Brink, Glen Gawarkiewicz, Rocky Geyer, Steven Lentz, Dennis McGillicuddy, Robert Todd, and John Trowbridge for helpful discussions during the course of the study or useful comments on earlier versions of the manuscript. The satellite sea surface temperature data were obtained from the University of Delaware Ocean Exploration, Remote Sensing, Biogeography Lab (led by Matthew Oliver), through the Mid-Atlantic Coastal Ocean Observing System (MARACOOS) data server (http://tds.maracoos.org/thredds/catalog.html). The OOI Pioneer Array mooring and glider data presented in this paper were downloaded from the National Science Foundation OOI data portal (http://ooinet.oceanobservatories.org) in July–August 2016.

References

Bisagni, J. J. (1983). Lagrangian current measurements within the eastern marin of a warm-core Gulf Stream ring. *Journal of Physical Oceanography*, *13*(4), 709–715. https://doi.org/10.1175/1520-0485(1983)013<0709:LCMWTE>2.0.CO;2

Brink, K. H. (1998). Deep sea forcing and exchange processes. In K. H. Brink, & A. R. Robinson (Eds.), *The global coastal ocean: Process and methods* (pp. 151–167). Cambridge, MA: Harvard University Press.

Capet, X., McWilliams, J. C., Molemaker, M. J., & Shchepetkin, A. F. (2008a). Mesoscale to submesoscale transition in the California Current System. Part I: Flow structure, eddy flux, and observational tests. *Journal of Physical Oceanography*, *38*(1), 29–43. https://doi.org/10.1175/2007JPO3671.1

Capet, X., McWilliams, J. C., Molemaker, M. J., & Shchepetkin, A. F. (2008b). Mesoscale to submesoscale transition in the California Current System. Part II: Frontal processes. *Journal of Physical Oceanography*, *38*(1), 44–64. https://doi.org/10.1175/2007JPO3672.1

Chapman, D. C., & Beardsley, R. C. (1989). On the origin of shelf water in the Middle Atlantic Bight. *Journal of Physical Oceanography*, *19*(3), 384–391. https://doi.org/10.1175/1520-0485(1989)019<0384:OTOOSW>2.0.CO;2

Chen, K., He, R., Powell, B. S., Gawarkiewicz, G. G., Moore, A. M., & Arango, H. G. (2014). Data assimilative modeling investigation of Gulf Stream Warm Core Ring interaction with continental shelf and slope circulation. *Journal of Geophysical Research: Oceans*, *119*, 5968–5991. https://doi.org/10.1002/2014JC009898

Cherian, D. A., & Brink, K. H. (2016). Offshore transport of shelf water by deep-ocean eddies. *Journal of Physical Oceanography*, *46*(12), 3599–3621. https://doi.org/10.1175/JPO-D-16-0085.1

Cherian, D. A., & Brink, K. H. (2018). Shelf flows forced by deep-ocean anticyclonic eddies at the shelfbreak. *Journal of Physical Oceanography*, *48*(5), 1117–1138. https://doi.org/10.1175/JPO-D-17-0237.1

Churchill, J. H., Cornillon, P. C., & Milkowski, G. W. (1986). A cyclonic eddy and shelf-slope water exchange associated with a Gulf Stream warm-core ring. *Journal of Geophysical Research*, *91*, 9615–9623. https://doi.org/10.1029/JC091iC08p09615

Early, J. J., Samelson, R. M., & Chelton, D. B. (2011). The evolution and propagation of quasigeostrophic ocean eddies. *Journal of Physical Oceanography*, *41*(8), 1535–1555. https://doi.org/10.1175/2011JPO4601.1

Fratantoni, P., Pickart, R., Torres, D., & Scotti, A. (2001). Mean structure and dynamics of the shelfbreak jet in the Middle Atlantic Bight during fall and winter. *Journal of Physical Oceanography*, *31*(8), 2135–2156. https://doi.org/10.1175/1520-0485(2001)031<2135:MSADOT>2.0.CO;2

Garfield, N., & Evans, D. L. (1987). Shelf water entrainment by Gulf Stream warm-core rings. *Journal of Geophysical Research*, *92*, 13,003–13,012. https://doi.org/10.1029/JC092iC12p13003

Gawarkiewicz, G., Bahr, F., Beardsley, R. C., & Brink, K. H. (2001). Interaction of a slope eddy with the shelfbreak front in the Middle Atlantic Bight. *Journal of Physical Oceanography*, *21*, 2783–2796.

Gawarkiewicz, G., Brink, K. H., Bahr, F., Beardsley, R. C., Caruso, M., Lynch, J., & Chiu, C.-S. (2004). A large-amplitude meander of the shelfbreak front in the Middle Atlantic Bight: Observations from the Shelfbreak PRIMER Experiment. *Journal of Geophysical Research*, *109*, C03006. https://doi.org/10.1029/2002JC001468

Gawarkiewicz, G. G., Linder, C. A., Lynch, J. F., Newhall, A. E., & Bisagni, J. J. (1996). A surface-trapped intrusion of slope water onto the continental shelf in the Mid-Atlantic Bight. *Geophysical Research Letters*, *23*, 3763–3766. https://doi.org/10.1029/96GL03427

Gula, J., Molemaker, M. J., & McWilliams, J. C. (2014). Submesoscale cold filaments in the Gulf Stream. *Journal of Physical Oceanography*, *44*(10), 2617–2643. https://doi.org/10.1175/JPO-D-14-0029.1

Hoskins, B. J. (1982). The mathematical theory of frontogenesis. *Annual Review of Fluid Mechanics*, *14*(1), 131–151. https://doi.org/10.1146/annurev.fl.14.010182.001023

Houghton, R. W., Aikman, F. III, & Ou, H. W. (1988). Shelf-slope frontal structure and crossshelf exchange at the New England shelfbreak. *Continental Shelf Research*, *8*(5-7), 687–710. https://doi.org/10.1016/0278-4343(88)90072-6

Houghton, R. W., Vaillancourt, R. D., Marra, J., Hebert, D., & Hales, B. (2009). Cross-shelf circulation and phytoplankton distribution at the summertime New England shelfbreak front. *Journal of Marine Systems*, *78*(3), 411–425. https://doi.org/10.1016/j.jmarsys.2008.11.023

Joyce, T. M. (1991). Review of U. S. contribution to Warm-core rings. *Reviews of Geophysics*, *29*(S2), 610–616. https://doi.org/10.1002/org.1991.29.s2.610

Joyce, T. M., Bishop, J. K. B., & Brown, O. B. (1992). Observations of offshore shelf-water transport induced by a warm-core ring. *Deep Sea Research*, *39*, S97–S113. https://doi.org/10.1016/S0198-0149(11)80007-5

Kennelly, M. A., Evans, R. H., & Joyce, T. M. (1985). Small-scale cyclones on the periphery of the Gulf Stream warm-core ring. *Journal of Geophysical Research*, *90*, 8845–8857. https://doi.org/10.1029/JC090iC05p08845

Kupferman, S. L., & Garfield, N. (1977). Transport of low-salinity water at the slope water-Gulf Stream boundary. *Journal of Geophysical Research*, *82*(24), 3481–3486. https://doi.org/10.1029/JC082i024p03481

Lentz, S. J. (2003). A climatology of salty intrusions over the continental shelf from Georges Bank to Cape Hatteras. *Journal of Geophysical Research*, *108*(C10), 3326. https://doi.org/10.1029/2003JC001859

Lentz, S. J. (2008). Observations and a model of the mean circulation over the Middle Atlantic Bight continental shelf. *Journal of Physical Oceanography*, *38*(6), 1203–1221. https://doi.org/10.1175/2007JPO3768.1

Levy, M., Klein, P., & Treguier, A.-M. (2001). Impact of sub-mesoscale physics on production and subduction of phytoplankton in an oligotrophic regime. *Journal of Marine Research*, *59*(4), 535–565. https://doi.org/10.1357/002224001762842181

Linder, C. A., & Gawarkiewicz, G. G. (1998). A climatology of the shelfbreak front in the Middle Atlantic Bight. *Journal of Geophysical Research*, *103*, 18,405–18,423. https://doi.org/10.1029/98JC01438

Mahadevan, A., & Tandon, A. (2006). An analysis of mechanisms for submesoscale vertical motion at ocean fronts. *Ocean Modelling*, *14*(3-4), 241–256. https://doi.org/10.1016/j.ocemod.2006.05.006

McDougall, T. J., Jackett, D. R., Millero, F. J., Pawlowicz, R., & Barker, P. (2012). A global algorithm for estimating absolute salinity. *Ocean Science*, *8*(6), 1123–1134. https://doi.org/10.5194/os-8-1123-2012

McWilliams, J. C. (2016). Submesoscale currents in the ocean. *Proceedings of the Royal Society A*, *472*(2189). https://doi.org/10.1098/rspa.2016.0117

McWilliams, J. C., Molemaker, M. J., & Olafsdottir, E. I. (2009). Line fluctuation growth during frontogenesis. *Journal of Physical Oceanography*, *39*(12), 3111–3129. https://doi.org/10.1175/2009JPO4186.1

Omand, M. M., D'Asaro, E. A., Lee, C. M., Perry, M. J., Briggs, N., Cetinie, I., & Mahadevan, A. (2015). Eddy-driven subduction exports particulate organic carbon from the spring bloom. *Science*, *348*(6231), 222–225. https://doi.org/10.1126/science.1260062

Schlitz, R. (2003). Interaction of shelf water with warm-core rings, focusing on the kinematics and statistics of shelf water entrained within streamers. NOAA Technical Memorandum NMFS-NE-170, 46 pp.

Shchepetkin, A. F., & McWilliams, J. C. (2008). Computational kernel algorithms for fine-scale, multiprocess, long-term oceanic simulations. In P. G. Ciarlet, R. Temam, & J. Tribbia (Eds.), *Handbook of numerical analysis. XIV: Computational methods for the atmosphere and the ocean* (pp. 121–183). New York: Elsevier Science.

Smith, K. S., & Ferrari, R. (2009). The production and dissipation of compensated thermohaline variance by mesoscale stirring. *Journal of Physical Oceanography*, *39*(10), 2477–2501. https://doi.org/10.1175/2009JPO4103.1

Smith, L. M., Barth, J. A., Kelley, D. S., Plueddemann, A., Rodero, I., Ulses, G. A., et al. (2018). The Ocean Observatories Initiative. *Oceanography*, *31*(1), 16–35. https://doi.org/10.5670/oceanog.2018.105

Spall, M. A. (1995). Frontogenesis, subduction, and cross-front exchange at upper ocean fronts. *Journal of Geophysical Research*, *100*, 2543–2557. https://doi.org/10.1029/94JC02860

Tang, C. L., Bennett, A. S., & Lawrence, D. J. (1985). Thermohaline intrusions in the frontal zones of a warm-core ring observed by Batfish. *Journal of Geophysical Research*, *90*, 8928–8942. https://doi.org/10.1029/JC090iC05p08928

Todd, R. E., Gawarkiewicz, G. G., & Owens, W. B. (2013). Horizontal scales of variability over the Middle Atlantic Bight shelfbreak and continental rise from finescale observations. *Journal of Physical Oceanography*, *43*(1), 222–230. https://doi.org/10.1175/JPO-D-12-099.1

Vaillancourt, R. D., Marra, J., Prieto, L., Houghton, R. W., Hales, B., & Hebert, D. (2005). Light absorption and scattering by particles and CDOM at the New England shelfbreak front. *Geochemistry, Geophysics, Geosystems*, *6*, Q11003. https://doi.org/10.1029/2005GC000999

Warner, J. C., Sherwood, C. R., Arango, H. G., & Signell, R. P. (2005). Performance of four turbulence closure models implemented using a generic length scale method. *Ocean Modelling*, *8*(1-2), 81–113. https://doi.org/10.1016/j.ocemod.2003.12.003

Zhang, W. G., & Gawarkiewicz, G. G. (2015a). Dynamics of the direct intrusion of gulf stream ring water onto the Mid-Atlantic Bight shelf. *Geophysical Research Letters*, *42*, 7687–7695. https://doi.org/10.1002/2015GL065530

Zhang, W. G., & Gawarkiewicz, G. G. (2015b). Length-scale of the finite-amplitude meanders of shelfbreak fronts. *Journal of Physical Oceanography*, *45*(10), 2598–2620. https://doi.org/10.1175/JPO-D-14-0249.1

Zhang, W. G., Gawarkiewicz, G. G., McGillicuddy, D. J., & Wilkin, J. L. (2011). Climatological mean circulation at the New England shelf break. *Journal of Physical Oceanography*, *41*(10), 1874–1893. https://doi.org/10.1175/2011JPO4604.1

Zhang, W. G., Wilkin, J. L., & Schofield, O. M. E. (2010). Simulation of water age and residence time in New York Bight. *Journal of Physical Oceanography*, *40*(5), 965–982. https://doi.org/10.1175/2009JPO4249.1